

# **Ion Permeation and Selectivity of OmpF Porin: A Theoretical Study Based on Molecular Dynamics, Brownian Dynamics, and Continuum Electrodiffusion Theory**

**Wonpil Im and Benoît Roux\***

*Department of Biochemistry  
Weill Medical College  
of Cornell University  
1300 York Avenue, Box 63  
New York, NY 10021, USA*

Three different theoretical approaches are used and compared to refine our understanding of ion permeation through the channel formed by OmpF porin from *Escherichia coli*. Those approaches are all-atom molecular dynamics (MD) in which ions, solvent, and lipids are represented explicitly, Brownian dynamics (BD) in which ions are represented explicitly, while solvent and lipids are represented as featureless dielectrics, and Poisson–Nernst–Planck (PNP) electrodiffusion theory in which both solvent and local ion concentrations are represented as a continuum. First, the ability of the different theoretical approaches in reproducing the equilibrium average ion density distribution in OmpF porin bathed by a 1 M KCl symmetric salt solution is examined. Under those conditions the PNP theory is equivalent to the non-linear Poisson–Boltzmann (PB) theory. Analysis shows that all the three approaches are able to capture the important electrostatic interactions between ions and the charge distribution of the channel that govern ion permeation and selectivity in OmpF. The  $K^+$  and  $Cl^-$  density distributions obtained from the three approaches are very consistent with one another, which suggests that a treatment on the basis of a rigid protein and continuum dielectric solvent is valid in the case of OmpF. Interestingly, both BD and continuum electrostatics reproduce the distinct left-handed twisted ion pathways for  $K^+$  and  $Cl^-$  extending over the length of the pore which were observed previously in MD. Equilibrium BD simulations in the grand canonical ensemble indicate that the channel is very attractive for cations, particularly at low salt concentration. On an average there is 1.55  $K^+$  inside the pore in 10 mM KCl. Remarkably, there is still 0.17  $K^+$  on average inside the pore even at a concentration as low as 1  $\mu$ M KCl. Secondly, non-equilibrium ion flow through OmpF is calculated using BD and PNP and compared with experimental data. The channel conductance in 0.2 M and 1 M KCl calculated using BD is in excellent accord with the experimental data. The calculations reproduce the experimentally well-known conductance–concentration relation and also reveal an asymmetry in the channel conductance (a larger conductance is observed under a positive transmembrane potential). Calculations of the channel conductance for three mutants (R168A, R132A, and K16A) in 1 M KCl suggest that the asymmetry in the channel conductance arises mostly from the permanent charge distribution of the channel rather than the shape of the pore itself. Lastly, the calculated reversal potential in a tenfold salt gradient (0.1:1 M KCl) is 27.4( $\pm$ 1.3) mV (BD) and 22.1( $\pm$ 0.6) mV (PNP), in excellent accord with the experimental value of 24.3 mV. Although most of the results from PNP are qualitatively reasonable, the calculated channel

Present address: W. Im, Department of Molecular Biology (TPC6), The Scripps Research Institute, 10550 North Torrey Pines Rd, La Jolla, CA 92037, USA.

Abbreviations used: MD, molecular dynamics; BD, Brownian dynamics; PB, Poisson–Boltzmann theory; PNP, Poisson–Nernst–Planck theory.

E-mail address of the corresponding author: [benoit.roux@med.cornell.edu](mailto:benoit.roux@med.cornell.edu)

conductance is about 50% higher than that calculated from BD probably because of a lack of some dynamical ion–ion correlations.

© 2002 Elsevier Science Ltd. All rights reserved

**Keywords:** ion channel; membrane protein; diffusion; reversal potential; ion flux

\*Corresponding author

## Introduction

OmpF porins are wide cation-selective aqueous pores found in the outer membrane of *Escherichia coli*. They serve to facilitate the translocations of hydrophilic solutes with molecular mass up to 600 Da across the outer membrane.<sup>1–3</sup> Although these pores appear to be relatively simple, they nonetheless exhibit interesting properties. In particular, OmpF is highly selective for cations at low salt concentration, but becomes weakly selective at concentration in the molar range.<sup>4–7</sup> Interestingly, exposure of *E. coli* to such high salt concentration triggers the expression of OmpC, an outer membrane porin which is stronger than OmpF in cation-selectivity.<sup>4,8</sup> The loss of selectivity at high salt concentration is generally thought to reflect the importance of ionic screening of the protein electrostatic field, though how this takes place at the microscopic level is unclear. In particular, the ion-accessible cross-sectional area in the most constricted region of OmpF is only about 15 Å<sup>2</sup>,<sup>9</sup> and the application of the concept of ionic screening in such a narrow space is questionable.<sup>10,11</sup> Because they are well-characterized, both structurally<sup>12</sup> and functionally,<sup>5,6</sup> OmpF and other porins represent ideal systems for addressing questions about the fundamental principles underlying ion flow in molecular pores.<sup>13,14</sup>

From a broader perspective, it is important to elucidate the microscopic factors governing the flow of ions through wide aqueous molecular pores because it is likely that those have a significant impact on the function of a number of biological channels. For example, low resolution electron microscopy images of the nicotinic acetylcholine receptor<sup>15</sup> or the Shaker K<sup>+</sup> channel<sup>16</sup> show that both channels possess a large complex cytoplasmic vestibule with windows through which ions must flow. An other particularly striking case is provided by the recently determined X-ray structure of the MthK potassium channel in a gated-open state.<sup>17</sup> The structure reveals that the entryway on the intracellular side is a wide aqueous vestibule of about 12 Å diameter (nearly 450 Å<sup>2</sup> cross sectional area). Remarkably, a very small residue (mostly alanine residue, sometimes glycine residue) positioned along the inner helices lining the edge of this wide vestibule is highly conserved in all K<sup>+</sup> channels for no other apparent reason than that a larger residue would present an unacceptable impediment to ion diffusion.<sup>17</sup> Consistent with this general idea, it has been suggested that the diffusion of K<sup>+</sup> into the intracellular entry-

way might explain the differences in conductances observed between a large variety of K<sup>+</sup> channels.<sup>18</sup> These intriguing observations suggest that ion flow, even within relatively wide aqueous vestibules, can have important biological consequences for the proper function of highly selective biological channels.

The goal of this paper is to refine our understanding of the fundamental principles governing ion diffusion through molecular pores. Theoretical models can help reaching this goal.<sup>19</sup> The combination of atomic resolution channel structures plus sophisticated numerical algorithms offers the possibility of a virtual route for interpreting and relating a channel structure to its function. Addressing questions about ion permeation and selectivity through molecular pores in a meaningful way is difficult, however, because it requires an ability to calculate ion fluxes with quantitative accuracy. Presently, these questions cannot be addressed with a unique approach. The complexity of biological channels requires a hierarchy of inter-related computational approaches corresponding to different levels of approximations. Which approach is best to use may depend on the microscopic detail of a particular channel, the specific questions being asked, and the limitations of computational resources. In the present study, three different theoretical approaches are used to investigate the permeation and selectivity of OmpF porin: molecular dynamics (MD), Brownian dynamics (BD), and Poisson–Nernst–Planck (PNP) electrodiffusion theory in full three-dimensional space. Let us first briefly review and contrast those approaches.

In MD simulations, the trajectory of all the atoms in a molecular system is generated by solving Newton's classical equations of motion numerically:<sup>20</sup>

$$m_i \ddot{\mathbf{r}}_i = - \frac{\partial U}{\partial \mathbf{r}_i} \quad (1)$$

where  $m_i$ ,  $\mathbf{r}_i$ , and  $\ddot{\mathbf{r}}_i$  are the mass, position, and acceleration of the  $i$ th atom, respectively, and  $U$  is the microscopic potential function of the system. Arguably, MD simulations with explicit ions, solvent, and membranes provide the most realistic representations of complex ion channel systems for studying ion permeation and selectivity. There have been a number of theoretical studies on ion permeation through OmpF using MD<sup>9,21,22</sup> as well as of other channels.<sup>23,24</sup> However, because the time-scale of the permeation process is significantly longer than what can currently achieved

with MD simulations, this approach is impractical for calculating statistically meaningful ion currents. Even in the case of the relatively wide OmpF channel, the translocation of a single  $K^+$  takes place in the order of a few nanoseconds (ns). Thus, it is necessary to rely on approaches that are simpler and computationally less expensive than fully detailed MD to calculate ion fluxes.

BD provides an attractive computational approach for simulating the permeation process through ion channels over long time-scales without having to treat a system in all atomic details explicitly.<sup>6,7,25–29</sup> In this approach, the channel and the ions are represented explicitly while the influence of the surrounding solvent molecules is incorporated implicitly *via* dissipative and stochastic random forces and some free energy potential. The stochastic trajectory of the ions is generated by:<sup>30,31</sup>

$$\dot{\mathbf{r}}_i(t) = -\frac{D_i}{k_B T} \frac{\partial \mathcal{W}}{\partial \mathbf{r}_i} + \boldsymbol{\zeta}_i(t) \quad (2)$$

where  $\mathbf{r}_i$  and  $\dot{\mathbf{r}}_i$  are the position and velocity of the  $i$ th ion,  $D_i$  is the diffusion constant,  $k_B T$  is the thermal energy,  $\boldsymbol{\zeta}_i(t)$  is a random gaussian noise, and  $\mathcal{W}$  is the multi-ion potential of mean force (PMF).<sup>32,33</sup> Schirmer and co-workers generated stochastic trajectories of isolated ions to examine the cation/anion specificity of OmpF and other porins.<sup>6,7</sup> Im & Roux also recently generated BD trajectories of OmpF with explicit multiple ions using a Grand Canonical Monte Carlo (GCMC) and BD algorithm to calculate the channel conductance.<sup>27,29</sup>

Both in the case of MD or BD, the properties of the system are extracted from time averages taken over atomistic trajectories; the trajectory is deterministic in the case of MD, whereas it is stochastic in the case of BD. A very different perspective is adopted by the Nernst–Planck continuum electrodiffusion theory which represents the average ion fluxes in terms of concentration and potential gradients.<sup>19</sup>

$$\mathbf{J}_\alpha(\mathbf{r}) = -D_\alpha(\mathbf{r}) \left( \nabla C_\alpha(\mathbf{r}) + \frac{C_\alpha(\mathbf{r})}{k_B T} \nabla \mathcal{W}_\alpha^{\text{eff}}(\mathbf{r}) \right) \quad (3)$$

where  $\mathbf{J}_\alpha(\mathbf{r})$  is the flux density of the ion of type  $\alpha$ ,  $C_\alpha(\mathbf{r})$  is the concentration, and  $\mathcal{W}_\alpha^{\text{eff}}(\mathbf{r})$  is the effective potential acting on the ions. The latter normally comprises a contribution from an electrostatic potential  $\phi(\mathbf{r})$  as well as from a core-repulsive potential  $U_{\text{core}}(\mathbf{r})$  excluding the ions from the interior of the protein or the membrane. The PNP theory is an approximation attempting to represent the average influence of those electrostatic interactions *via* the Poisson equation:

$$\nabla \cdot [\epsilon(\mathbf{r}) \nabla \phi(\mathbf{r})] = -4\pi \left( \rho_p(\mathbf{r}) + \sum_\alpha q_\alpha C_\alpha(\mathbf{r}) \right) \quad (4)$$

where  $\epsilon(\mathbf{r})$  is the space-dependent dielectric constant,  $q_\alpha$  is the ion charge, and  $\rho_p(\mathbf{r})$  is the charge

density of the channel protein.<sup>34,35</sup> Because the Nernst–Planck equation (3) and the Poisson equation (4) are coupled partial differential equations, they must be solved in a self-consistent manner for the electrostatic potential  $\phi(\mathbf{r})$  and ion concentrations  $C_\alpha(\mathbf{r})$ . For this reason, PNP is often referred to as a “mean-field theory”. Under equilibrium conditions in the absence of any net flux (i.e.  $\mathbf{J}_\alpha(\mathbf{r}) = 0$  for all  $\alpha$ ), the PNP theory becomes equivalent to the non-linear Poisson–Boltzmann (PB) continuum theory.<sup>36,37</sup>

$$\begin{aligned} & \nabla \cdot [\epsilon(\mathbf{r}) \nabla \phi(\mathbf{r})] \\ &= -4\pi \left( \rho_p(\mathbf{r}) + \sum_\alpha q_\alpha C_\alpha^{\text{bulk}} e^{-U_{\text{core}}(\mathbf{r})/k_B T} e^{-q_\alpha \phi(\mathbf{r})/k_B T} \right) \end{aligned} \quad (5)$$

where  $C_\alpha^{\text{bulk}}$  is the bulk concentration of the ions. Kurnikova *et al.* have developed an efficient numerical method to solve the PNP theory in three-dimensional space and have applied it to ion conduction through the gramicidin channel.<sup>38</sup> Results from a reduced one-dimensional theory (1D-PNP) applied to OmpF and its mutant G119D have been reported,<sup>39</sup> though to the best of our knowledge, no application of PNP to a large complex macromolecular channel such as OmpF porin has been published so far.

To some degree, one might expect that MD, BD, PB and PNP should all be able to contribute in refining our understanding of ion permeation. Nonetheless, there has been and continues to be a lack of consensus concerning the relative merits and limits of these different approaches.<sup>40–44</sup> Approximate theories such as BD, PB, and PNP are very attractive because they are less computationally intensive than all-atom MD. For this reason, these approaches have contributed, in large part, to the current view of the ion-conducting properties of porins.<sup>6,7,27,29,39,45–47</sup> But the validity of the continuum dielectric description of water in BD and PB in the context of a molecular pore such as OmpF is still unknown. Mean-field approaches such as PB or PNP ignore some ion–ion correlations and are, thus, intrinsically more approximate than BD. Furthermore, Chung and co-workers compared PB and PNP with BD in various simple model channels, and argued that there should be large discrepancies between BD and PB or PNP because the latter overestimates the shielding effect by counterions inside a pore.<sup>10,11</sup> Correspondingly, subtle details concerning the hydration of charged and polar species incorporated in all-atom MD are lost when the solvent is represented as a continuum dielectric medium as in BD simulations. Lastly, BD, PB, and PNP treat the protein as a rigid structure and the influence of thermal atomic fluctuations (included in MD) is neglected.

To insure that meaningful conclusions can be drawn from computational studies, the construction

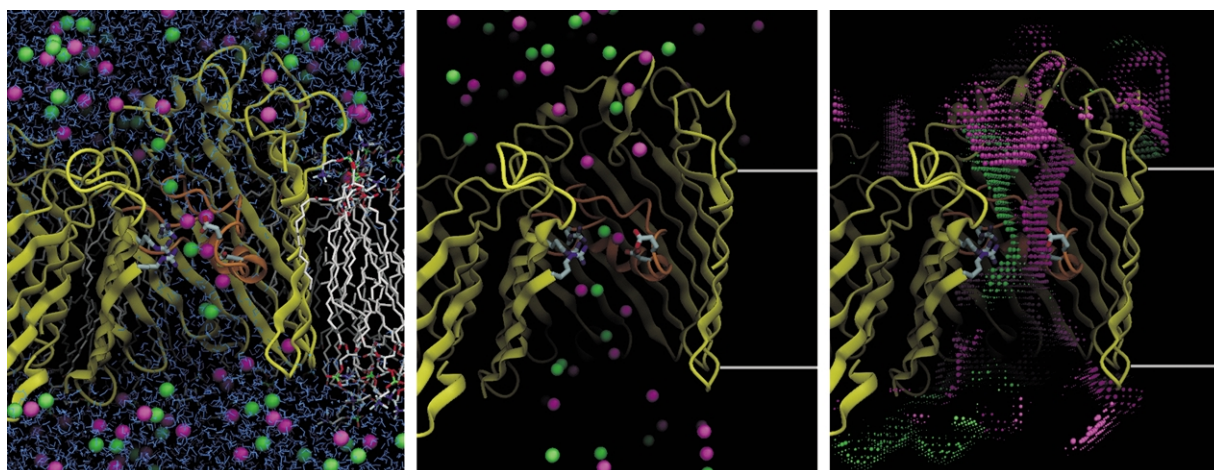


**Figure 1.** Graphics illustrations of various permeation model systems of OmpF porin. For a clear view of ion distribution inside the pore, one OmpF monomer and some atoms in the centered monomer were removed from the front view. The  $K^+$  are magenta and the  $Cl^-$  are green. The infolding loop L3 is colored by orange to show the constriction zone where the arginine cluster (Arg42, Arg82, and Arg132) and two acidic residues (Asp113 and Glu117) on L3 are shown as ball-and-stick models. (Left) MD system of OmpF embedded in a DMPC membrane solvated by a 1 M KCl aqueous salt solution. For clarity, some lipid molecules were removed from the front view. This snapshot was taken at 3.85 ns of the production run. (Middle) BD system of OmpF with an ion-impermeable planar membrane (gray line). (Right) PB (or PNP) system of OmpF with an ion-impermeable planar membrane (gray line). The net charge distribution ( $\rho(r) = \rho_K(r) - \rho_{Cl}(r)$ ) on a 3D-grid is shown; magenta only for  $\rho(r) > 1$  M and green only for  $\rho(r) < -1$  M. A larger grid size represents a higher density. The Figures were produced with DINO (A. Philippsen, DINO: visualizing structural biology, <http://www.dino3d.org>).

of a model, at any level of approximation, should ultimately be guided by the information extracted from more detailed representations. In the present study, we use the information extracted from a 5 ns equilibrium MD simulation of OmpF embedded in an explicit bilayer membrane bathed by a 1 M KCl aqueous salt solution<sup>9</sup> to provide the fundamental basis for constructing BD, PB, and PNP models that are as microscopically realistic as possible. In particular, the MD trajectory is used to characterize the effective diffusion constant of ions in the pore, and the ion-exclusion hydration layer near protein atoms. The approximate BD and (non-linear) PB are validated by examining their ability to reproduce the equilibrium properties from the MD simulation. The non-equilibrium ion fluxes through the channel are then calculated with BD and PNP and compared with available experimental data.

## Results and Discussion

We first compare the equilibrium average ion density distribution in OmpF porin calculated using MD, BD, and (non-linear) PB in the case of a 1 M KCl symmetric salt solution. The purpose of this comparison is to insure that the approximation that are being used in BD and PNP are sufficiently accurate to allow us to draw meaningful conclusion about ion permeation and selectivity in OmpF. Then, non-equilibrium ion fluxes through the channel are calculated with BD and PNP and compared. Various symmetric solutions of 0.01 M,

0.1 M, 0.2 M, 0.3 M, 0.5 M, 1 M, and 2 M KCl in the presence of an applied transmembrane potential are considered. Lastly, the non-equilibrium reversal potential is calculated using BD and PNP in the case of a tenfold salt gradient (0.1:1 M KCl) to characterize the selectivity of OmpF.

### Equilibrium ion distribution

In Figure 1 are shown molecular graphics views of OmpF porin bathed by a 1 M KCl salt solution according to MD,<sup>9</sup> BD, and PB. Figure 2 shows the equilibrium ion distribution for  $K^+$  and  $Cl^-$  inside the single-channel pore along the Z-axis. The average number of ions inside the pore are 5.1  $K^+$  and 3.9  $Cl^-$  (MD), 4.9  $K^+$  and 2.8  $Cl^-$  (BD), and 5.6  $K^+$  and 3.4  $Cl^-$  (PB), respectively. All three computational approaches show that  $K^+$  has a higher propensity to occupy the aqueous pore than  $Cl^-$ , consistent with the cation-selectivity of the OmpF channel.<sup>5</sup> In the narrow constriction zone and extracellular side, MD yields slightly higher densities of both  $K^+$  and  $Cl^-$  than those from BD or PB. In the periplasmic side of the pore, it yields lower densities of  $K^+$  and higher densities of  $Cl^-$  than those from BD or PB. These differences may result from a limited convergence of the configurational sampling for ion distribution in MD.<sup>9</sup> Nonetheless, the agreement is quite reasonable between MD and BD, indicating that the continuum dielectric description of water with a rigid channel structure in BD can be a valid approximation for OmpF porin. In contrast, such a good agreement with MD was not observed in our



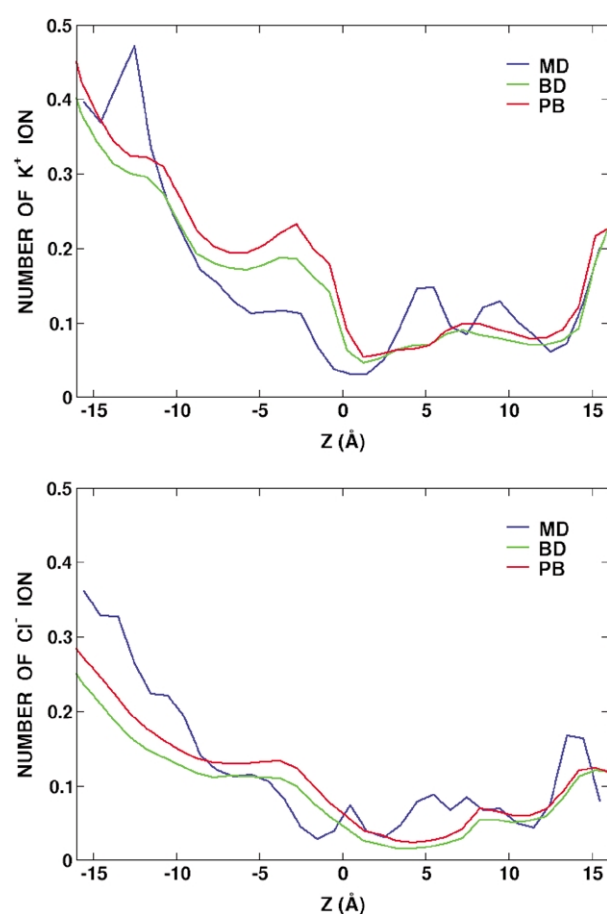


**Figure 2.** Average number of ions inside the channel pore along the Z-axis. MD results represent the average of all ions in three pores. The OmpF channel pore, here defined as the part of the channel bounded by the edges of the  $\beta$ -barrel, spans from  $-16$  Å to  $+16$  Å along the Z-axis. Three main regions can be distinguished: the wide intracellular vestibule ( $-16$  Å  $< Z < 2$  Å), the narrow constriction zone ( $2$  Å  $< Z < 6$  Å), and the extracellular vestibule ( $6$  Å  $< Z < 16$  Å). The number of ions was calculated using a  $1.0$  Å bin along the Z-axis.

previous BD simulations,<sup>27</sup> which were performed without solvent reaction field (see also equation (7) and work by Im & Roux<sup>29</sup>). Furthermore, the agreement between BD and PB is quite remarkable even though the ions are treated explicitly in the former and implicitly *via* a mean-field theory in the latter.

In a 5 ns MD trajectory,<sup>9</sup> it was previously observed that  $K^+$  and  $Cl^-$  follow two well-separated average pathways spanning over nearly 40 Å along the axis of the pore. In the center of the monomer, the two screw-like pathways have a left-handed twist, undergoing a counter-clockwise rotation of  $180^\circ$  from the extracellular vestibule to the pore periplasmic side. To investigate the extent to which the simpler approaches reproduce this specific feature of the pore observed in MD, we examined a superimposition of instantaneous configurations of ions from BD and a 3D-grid map of ion distribution from PB. The results are shown in

**Figure 3.** Remarkably, BD and PB reproduce the well-separated ion pathways, although the screw-like pathway in BD and PB is not as clear as in MD. This seems to suggest that MD samples narrower range of configurations than BD or PB. For a clearer comparison, average ion densities in the XY cross-sectional plane were calculated at three different positions along the Z-axis; the extracellular vestibule, the constriction zone, and the pore periplasmic side. They are shown in **Figure 4**. In the extracellular vestibule, a high density of  $K^+$  ions is observed at the outer rim of the  $\beta$ -barrel (above Asp113, Glu117, and Asp121 on loop L3). The region of high  $Cl^-$  density, well separated from that of  $K^+$ , is found near Arg167 and Arg168. The charge separation in the constriction zone is caused by the strong transversal electrostatic field generated between the arginine cluster (Arg42, Arg82, and Arg132) and two acidic residues (Asp113 and Glu117) on L3.<sup>6,9,12,27,45,47</sup> On the periplasmic side of the pore, there is an abrupt increase in the ion accessible area and a high density of  $Cl^-$  is observed between Lys16 and Arg270 in MD, around Lys16 in BD, or between Lys16 and Lys46 in PB. A high density of  $K^+$  ions is observed at the outer rim of the  $\beta$ -barrel. Overall, the ion-accessible space and the charge separation between MD and BD (or PB) are quite similar. The existence of two well-separated pathways for cations and anions suggests that the charge specificity of OmpF porin does not arise from a few local interactions in the constriction zone, but rather from a number of residue distributed over a large fraction of the aqueous pore.<sup>9</sup> The present analysis shows that BD and PB as well are also able to capture the important electrostatic interactions between ions and the charge distribution of OmpF.

On the basis of a comparison of PB and PNP with BD in various simple model pores, Chung and co-workers argued that there should be large discrepancies between BD and so-called mean-field theories such as PB or PNP because the latter overestimates the shielding effect by counterions due to underestimation of the self-energy in narrow channels.<sup>10,11</sup> Such a large discrepancy between the two theories is not observed in the present calculations, presumably because the pore of OmpF is sufficiently wide and the electric field arising from the fixed charges of the protein atoms is relatively strong. It should be noted, nevertheless, that the reaction field in BD has an important influence on energetics and ion distribution inside the pore.<sup>29</sup> For example, when the reaction field is turned off in BD, the average number of  $K^+$  inside the pore increases from 4.6 to 9.1 while that of  $Cl^-$  remains almost unchanged.

### Non-equilibrium ion flow: channel conductance and selectivity

Because it is not feasible yet to calculate statistically meaningful ion fluxes directly from MD

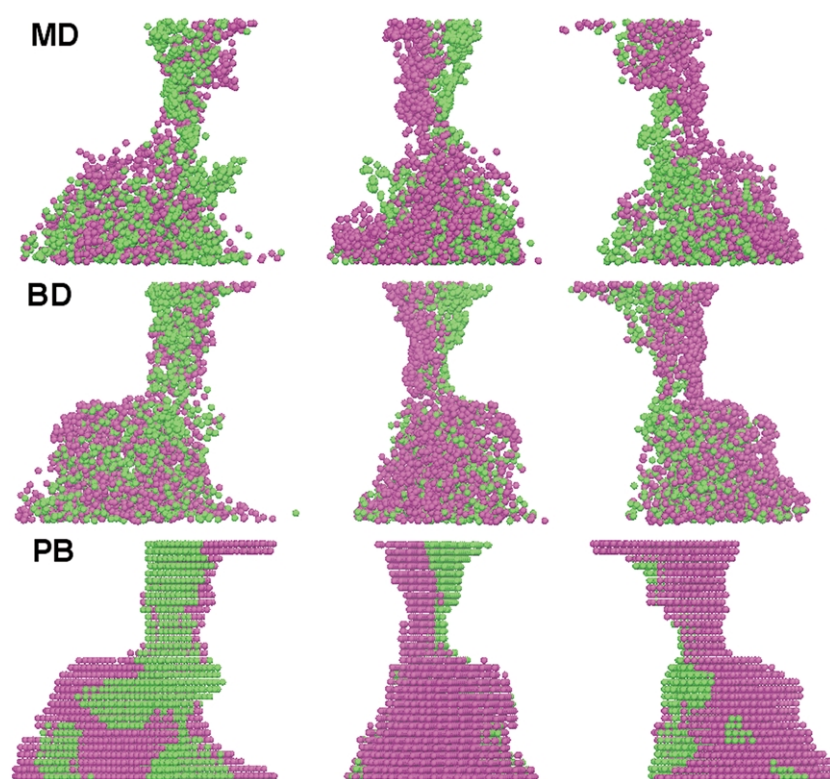


**Figure 3.** Two well-separated specific ion pathways with a left-handed screw-like fashion. The  $K^+$  are magenta and the  $Cl^-$  are green. (MD) A superimposition of 100 snapshots of ions every 50 ps from the 5 ns trajectory. All the ions in two other pores were superimposed into one pore by rotations. (BD) A superimposition of 300 snapshots of ions every 60 ps from the 60 ns trajectory. (PB) An ion distribution 3D-grid map. (Left) View from perpendicular to the threefold symmetric axis. (Middle) Left view rotated by  $120^\circ$ . (Right) Left view rotated by  $240^\circ$ . The Figure was produced with DINO (A. Philippsen, DINO: visualizing structural biology, <http://www.dino3d.org>).

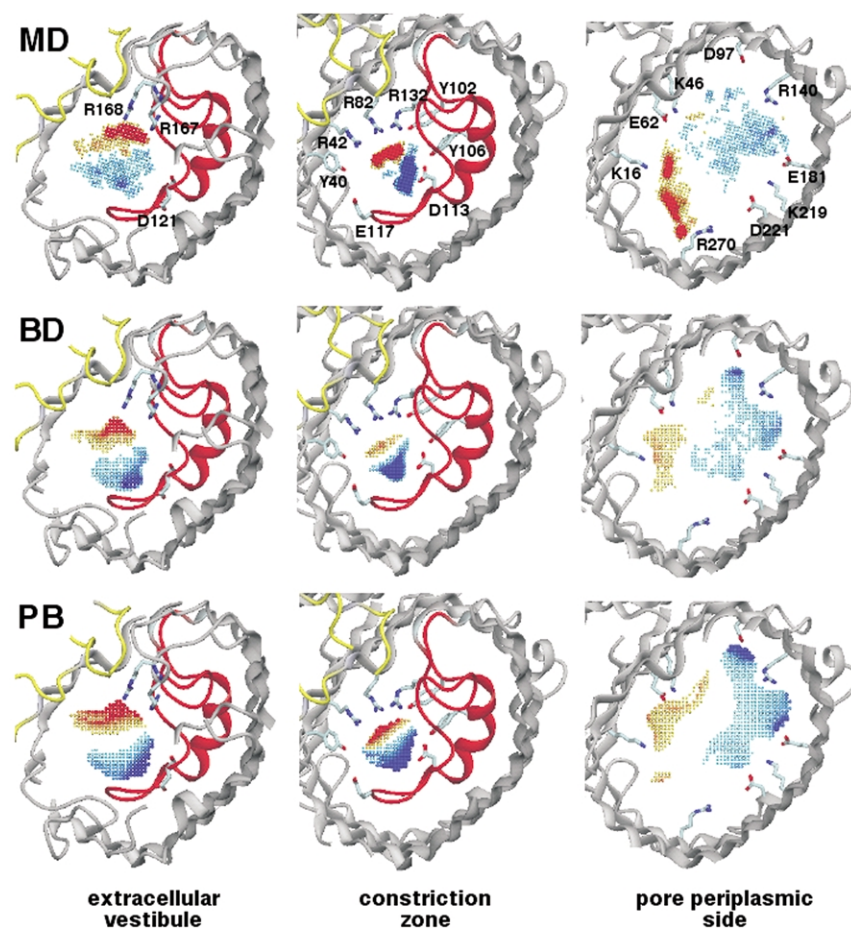


**Figure 4.** Ion density maps on the XY plane at the different positions along the Z-axis, calculated using a  $93 \times 93 \times 5$  grid (with grid-spacing of  $0.5 \text{ \AA}$ ) corresponding to a slab of  $2.5 \text{ \AA}$  thickness; (left) in the extracellular vestibule (between  $Z = 14.25 \text{ \AA}$  and  $Z = 11.75 \text{ \AA}$ ), (middle) in the constriction zone (between  $Z = 5.25 \text{ \AA}$  and  $Z = 2.75 \text{ \AA}$ ), and (right) in the pore periplasmic side (between  $Z = -2.75 \text{ \AA}$  and  $Z = -5.25 \text{ \AA}$ ). The  $K^+$  density  $\rho_{K^+}$  (parts./ $\text{\AA}^3$ ) is represented by cyan ( $\rho_{K^+} = 0.0006$ ) to blue ( $\rho_{K^+} = 0.003$ ) and the  $Cl^-$  density  $\rho_{Cl^-}$  (parts./ $\text{\AA}^3$ ) by yellow ( $\rho_{Cl^-} = 0.0006$ ) to red ( $\rho_{Cl^-} = 0.003$ ). MD represents the average density of all three pores from the 5 ns trajectory and BD represents that from the 60 ns trajectory. The key residues are shown as labeled ball-and-stick models. The Figures were produced with DINO (A. Philippsen, DINO: visualizing structural biology, <http://www.dino3d.org>).

**Table 1.** Conductance (nS) and current ratios from GCMC/BD simulations and PNP calculations of OmpF porin in various KCl symmetric solutions

	$V_{mp} = +150$ mV		$V_{mp} = -150$ mV		
Concentration	$G_+$	$I_K/I_{Cl}$	$G_-$	$I_K/I_{Cl}$	$G_+/G_-$
GCMC/BD					
2.00	$2.21 \pm 0.08$	1.24	$1.94 \pm 0.12$	1.33	1.14
1.00	$1.36 \pm 0.06$	1.38	$1.15 \pm 0.05$	1.62	1.18
0.50	$0.81 \pm 0.03$	1.82	$0.61 \pm 0.03$	2.30	1.31
0.30	$0.55 \pm 0.02$	2.58	$0.40 \pm 0.02$	3.52	1.37
0.20	$0.42 \pm 0.02$	3.67	$0.31 \pm 0.01$	5.41	1.35
0.10	$0.32 \pm 0.01$	7.96	$0.23 \pm 0.01$	14.34	1.37
0.01	$0.22 \pm 0.01$	346.12	$0.16 \pm 0.01$	1147.95	1.38
PNP					
2.00	$3.45 \pm 0.06$	1.10	$3.25 \pm 0.06$	1.13	1.07
1.00	$1.97 \pm 0.04$	1.20	$1.77 \pm 0.03$	1.27	1.12
0.50	$1.15 \pm 0.02$	1.43	$0.97 \pm 0.02$	1.59	1.19
0.30	$0.78 \pm 0.02$	1.77	$0.63 \pm 0.01$	2.12	1.24
0.20	$0.59 \pm 0.02$	2.23	$0.46 \pm 0.01$	2.94	1.28
0.10	$0.38 \pm 0.01$	4.03	$0.30 \pm 0.01$	6.44	1.26
0.01	$0.23 \pm 0.01$	117.96	$0.20 \pm 0.01$	557.10	1.14

simulations at the present time, we investigated non-equilibrium ion flow through OmpF porin using BD and PNP. In Table 1 are summarized the characteristics of the single-channel conductance ( $G = I/V$ ) and ion current ratios ( $I_K/I_{Cl}$ ) through OmpF porin in various symmetric KCl salt solutions with transmembrane potentials  $V_{mp} = \pm 150$  mV. Error bars in BD results represent the

root-mean-square (RMS) fluctuation of ten independent trajectories and those in PNP results represent the variation (convergence error) of the current  $I_\alpha(z)$  (see Theory and Methods). The small variations in PNP demonstrate that the present numerical scheme is robust and ion currents are numerically well converged.

The current–voltage ( $I$ – $V$ ) relation in 1 M KCl is shown in Figure 5. In both BD and PNP calculations, more currents are carried by  $K^+$  than  $Cl^-$ , consistent with the cation-selectivity of the channel.<sup>5</sup> The  $I$ – $V$  relation appears to be asymmetric, i.e. both  $I_K$  and  $I_{Cl}$  at a positive potential are always larger than those at the corresponding negative potential, resulting in the asymmetry in the channel conductance upon the polarity of the applied potential (see also Table 1). A similar  $I$ – $V$  relation is also found in 0.01 M and 0.1 M KCl (data not shown).

The measured conductance of OmpF inserted in a planar lipid bilayer in 1 M KCl solution is  $1.25(\pm 0.16)$  nS at  $V_{cis} = -160$  mV, and  $1.13(\pm 0.16)$  nS at  $V_{cis} = +160$  mV (the *trans* compartment is grounded, i.e.  $V_{trans} = 0$  mV; N. Saint, personal communication). In those experiments, approximately six OmpF trimers added to the *cis* compartment randomly insert into the lipid bilayer. Though the exact orientation of each trimer is unknown, it seems likely that for most channels the short periplasmic loops of the porins first insert into the bilayer leaving the long extracellular loops on the *cis* side (N. Saint, personal communication). According to this analysis, in which a positive potential  $V_{cis}$  in the experiments corresponds to a negative potential applied in the calculations, the slight asymmetry observed in the experiments and in the calculations are consistent. This is further supported by recent results using the patch-clamp technique in which the *in vivo* orientation of the channel is known,<sup>48</sup> a similar asymmetry in the channel conductance was observed in 0.2 M KCl, i.e.  $0.34(\pm 0.03)$  nS at  $V_{mp} > +150$  mV and

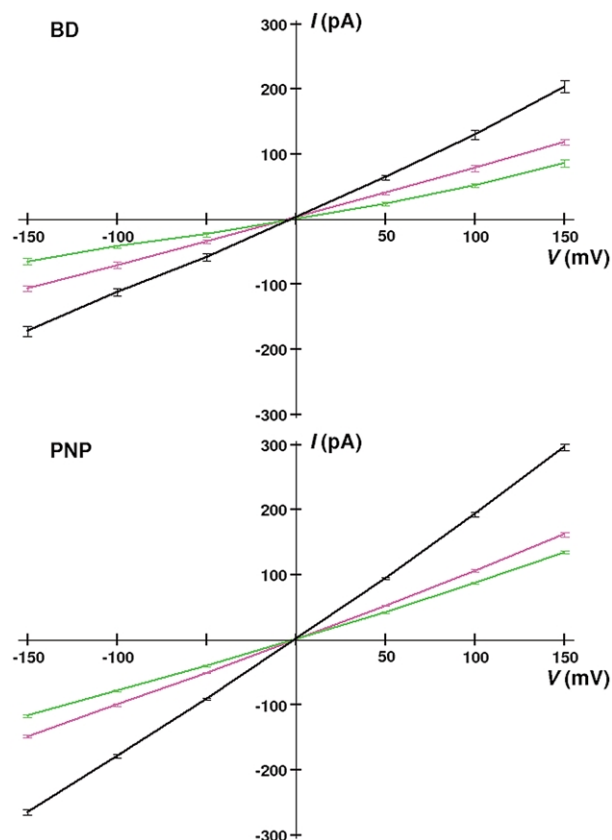


**Figure 5.** Current–voltage curve in a 1 M KCl symmetric solution from BD simulations (top) and PNP calculations (bottom). The total current (black) is the sum of  $K^+$  (magenta) and  $Cl^-$  (green) currents.



**Table 2.** Ion currents (pA) and conductance (nS) from GCMC/BD simulations of OmpF and its mutants in a 1 M KCl symmetric solution

Protein	$V_{mp} = +150$ mV			$V_{mp} = +150$ mV			
	$I_K(+)$	$I_{Cl}(-)$	$G_+$	$I_K(-)$	$I_{Cl}(+)$	$G_-$	$G_+/G_-$
OmpF, uncharged <sup>a</sup>	$54.4 \pm 2.2$	$54.8 \pm 5.2$	$0.73 \pm 0.04$	$-56.3 \pm 2.8$	$-55.8 \pm 3.8$	$0.75 \pm 0.03$	0.97
OmpF	$117.9 \pm 4.2$	$85.7 \pm 5.8$	$1.36 \pm 0.06$	$-106.4 \pm 4.0$	$-65.5 \pm 5.0$	$1.15 \pm 0.05$	1.18
R168A	$117.4 \pm 3.1$	$62.1 \pm 5.3$	$1.20 \pm 0.04$	$-124.6 \pm 5.3$	$-61.8 \pm 3.3$	$1.24 \pm 0.05$	0.96
R132A	$145.1 \pm 4.1$	$56.6 \pm 4.8$	$1.34 \pm 0.05$	$-122.5 \pm 5.6$	$-39.8 \pm 3.7$	$1.08 \pm 0.06$	1.24
K16A	$170.5 \pm 5.9$	$68.7 \pm 3.5$	$1.59 \pm 0.06$	$-110.9 \pm 5.7$	$-33.6 \pm 4.7$	$0.96 \pm 0.06$	1.66

$I_\alpha(+)$  and  $I_\alpha(-)$  are the outward and inward currents of the ion of type  $\alpha$ , respectively.

<sup>a</sup> BD results with all protein charges turned off.

0.27( $\pm 0.05$ ) ns at  $V_{mp} < -150$  mV. Although the conductance and its asymmetry calculated from BD is slightly higher than the experimental data, the agreement in 0.2 M and 1 M KCl is excellent, given the fact that no parameters were specifically adjusted to match those experimental data. (In fact, the calculations in 0.2 M were performed before we had access to the data.)

Table 1 shows the variation of the asymmetry in the channel conductance upon the polarity of the applying potential ( $G_+/G_-$ ) as a function of concentrations. The asymmetry appears to increase with decreasing salt concentration, except the PNP result in 0.01 M. What could be the microscopic origin for the asymmetric channel conductance? Does it mainly arise from the irregular shape of the channel shown in Figure 3, or from the permanent charge distribution of the channel? To examine the influence of the asymmetric shape of the channel, BD simulations were performed with the all protein charges turned off. The results, given in Table 2, clearly show that the channel geometry itself has almost no influence on the asymmetric channel conductance (within the statistical errors). Furthermore, it is clearly shown that the permanent charge distribution of OmpF porin attracts more  $K^+$  in the periplasmic side than in the extracellular side, resulting in higher (outward)  $K^+$  current at positive transmembrane potential and lower (inward)  $K^+$  current at negative potential. The opposite is true for  $Cl^-$ .

Interestingly, although BD and PB are in excellent accord for equilibrium situations, Figure 5 and Table 1 show that the ionic currents calculated from PNP are always larger than those from BD simulations. Since all the microscopic model and input parameters are all identical here, the difference between BD and PNP is obviously caused by the mean-field approximation in which some dynamical ion-ion correlations are neglected. As shown in Figure 6, the BD simulation at  $V_{mp} = +150$  mV clearly shows strong ion-counterion correlations in the constriction zone of OmpF. The passage of  $Cl^-$  always depends on the presence of  $K^+$ , whereas isolated  $K^+$  can permeate on their own. This is consistent with the fact that a significant amount of ion-ion pairing was previously observed in the narrowest region of the OmpF

pore during MD simulation.<sup>9</sup> In bulk solution, it is known that such correlations which increase with ion concentration result in a small reduction of the effective ion diffusion constant.<sup>49</sup> Correlations are particularly important here because the ion concentration inside the molecular pore is much higher than the bulk concentration, e.g. in 1 M KCl solution both  $K^+$  and  $Cl^-$  concentrations in the constriction zone of OmpF are more than 5 M, as shown in Figure 4. Thus, a significant reduction of ion mobility that is not captured in PNP is expected inside the pore. Consistent with this view, a higher conductance is obtained when the short-range ion-ion interaction  $w_{sr}(r)$  is neglected in BD; 1.57( $\pm 0.07$ ) ns at  $V_{mp} = +150$  mV. To mimic the influence of ion-ion correlations implicitly, an empirical scaling factor of the ion diffusion constant could be used inside the pore in PNP calculations. For example, when the minimum fraction  $f_{min}$  in the diffusion profile of the ions, shown in Figure 11, is reduced from 0.5 to 0.3, the conductance reduces to 1.30( $\pm 0.04$ ) ns

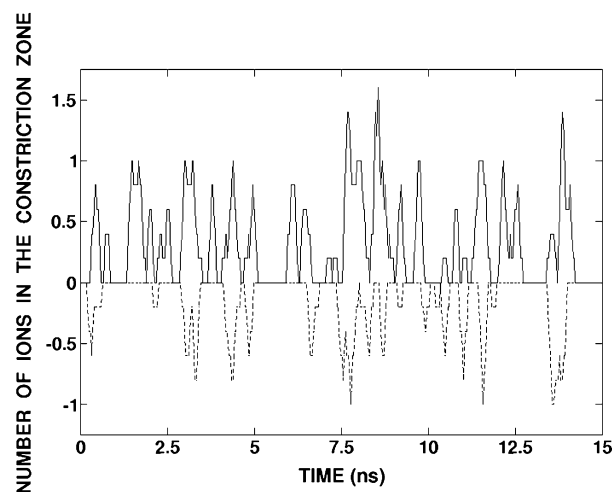


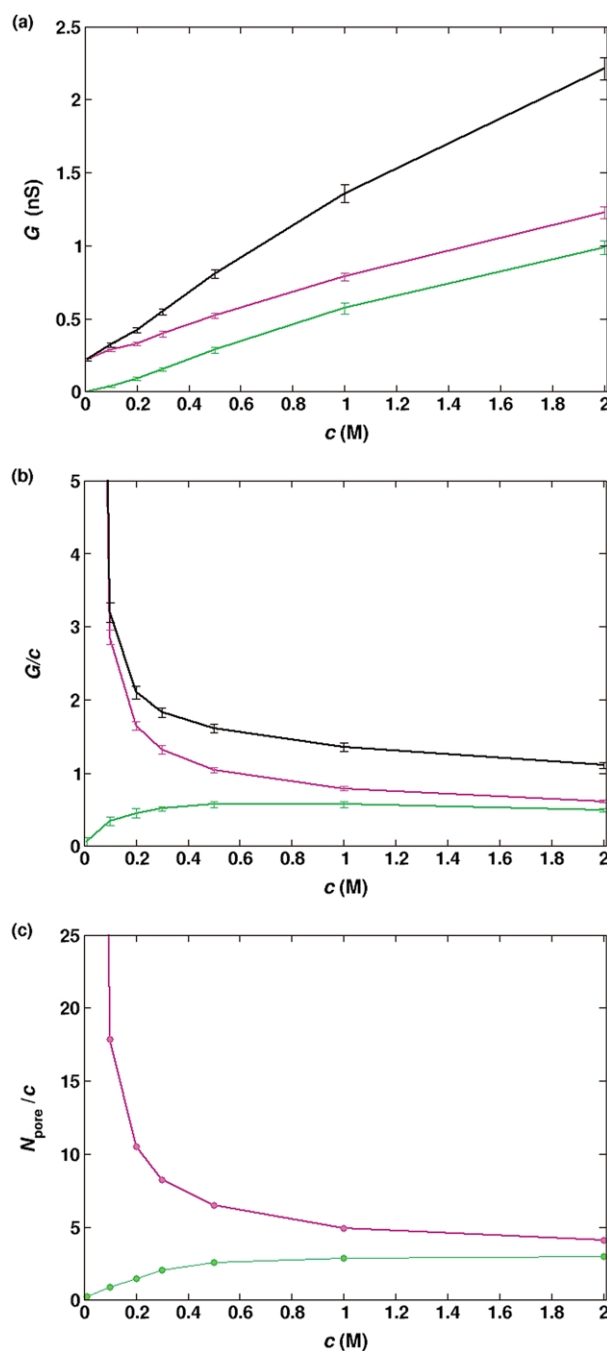
**Figure 6.** Average number of  $K^+$  (continuous line) and  $Cl^-$  (broken line) in the constriction zone of OmpF which corresponds to  $2.5 \text{ \AA} < Z < 6 \text{ \AA}$ . The average is taken over a time interval of 75 ps from the BD simulation in 1 M KCl with  $V_{mp} = +150$  mV. A strong ion-counterion correlation is clearly shown in the constriction zone.



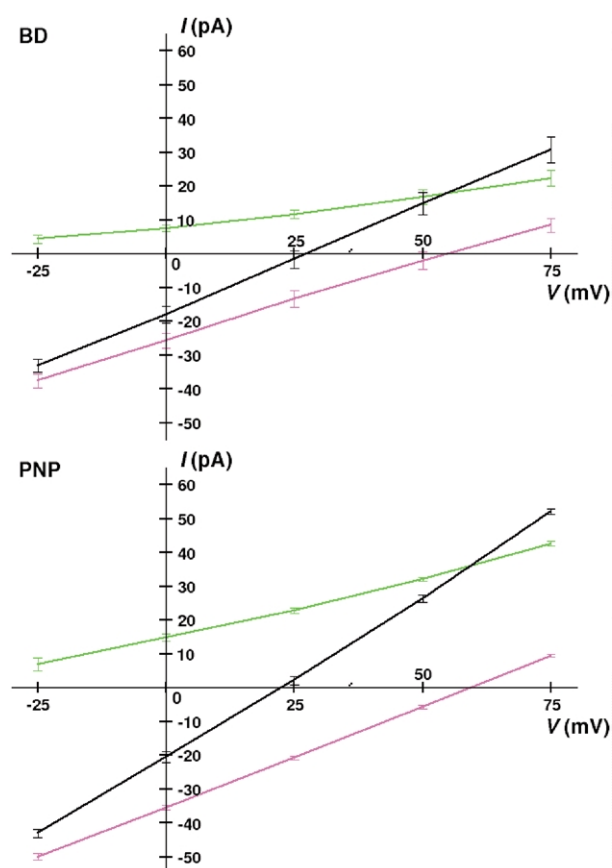
at  $V_{mp} = +150$  mV and  $1.18(\pm 0.03)$  ns at  $V_{mp} = -150$  mV, which are now quite similar to the corresponding BD results.

Table 1 shows the variation of channel conductance at  $V_{mp} = \pm 150$  mV as a function of concentrations. Figure 7(a) shows the conductance–concentration relation which appears to be sublinear at high concentrations. Figure 7(b) shows that the single-channel conductance normalized by salt concentration ( $G/c$ ) increases sharply with decreasing ionic strength, as observed experimentally.<sup>6</sup> Assuming that the current ratio  $I_K/I_{Cl}$  is representative of the channel selectivity at a given concentration, OmpF becomes increasingly more selective for  $K^+$  and excludes  $Cl^-$  as the concentration is decreased because of the reduction of ionic screening of the negative electrostatic potential arising from the protein charges. OmpF becomes highly cation-selective in a physiological concentration of 0.1 M KCl. In fact, the variation of  $G/c$  is well correlated with the variation of the number of  $K^+$  and  $Cl^-$  inside the pore normalized by salt concentration  $N_{pore}/c$ , as shown in Figure 7(c). In particular, there are 1.55  $K^+$  inside the pore in 0.01 M, which is only about three times smaller than the number of  $K^+$  in 1 M KCl, whereas the number of  $Cl^-$  is then almost negligible (additional simulations indicate that there is still roughly 0.17  $K^+$  on average inside the pore even in 1  $\mu$ M). As a result, the conductance at low concentration is significantly larger than a simple naive extrapolation from the value at high concentration would suggest. Qualitatively similar results are also obtained from PNP for Figure 7(a)–(c) (data not shown).

What is the origin of the charge specificity of OmpF is perhaps the most important question in addressing the relation of structure to function for this ion conducting pore. The observation of well-separated cationic and anionic screw-like pathway extending over a significant fraction of the pore suggests that charge specificity might arise from a number of residues. To illustrate the influence of key basic residues on the anionic screw-like pathway shown in Figure 4, we performed BD simulations for three mutants; R168A (located at  $Z = 15.5$  Å in the extracellular vestibule), R132A (located at  $Z = 3$  Å near the constriction zone), and K16A (located at  $Z = -1$  Å on the periplasmic side of the pore). It was assumed that the ions inside the pores of the mutants follow the same ion diffusion profiles as in OmpF (see Figure 11). The results are summarized in Table 2. Compared to wide-type OmpF, all the mutants show various increase in the  $K^+$  current and decrease in the  $Cl^-$  current depending on positions and environment of the mutations, thus resulting in various increase of cation-selectivity. The asymmetry in the channel conductance is also affected by the mutations of the key basic residues. The sequence of  $G_+/G_-$  is K16A > R132A > OmpF > R168A. In particular, R168A shows higher inward  $K^+$  current  $I_K(-)$  and lower inward  $Cl^-$  current



**Figure 7.** (a) Conductance–concentration ( $G$ – $c$ ) relation (black) from BD at  $V_{mp} = +150$  mV. The contributions from  $K^+$  (magenta) and  $Cl^-$  (green) are also shown. (b) Channel conductance normalized by salt concentration  $G/c$  (black) versus concentration from BD at  $V_{mp} = +150$  mV. The contributions from  $K^+$  (magenta) and  $Cl^-$  (green) are also shown. For clarity, values for  $G/c$  (22.22) and the  $K^+$  contribution (22.15) at 0.01 M are not shown. (c) Number of  $K^+$  (magenta) and  $Cl^-$  (green) inside pore normalized by salt concentration  $N_{pore}/c$  versus concentration from BD without transmembrane potential. For clarity, a value for  $N_{pore}/c$  (155.17) at 0.01 M is not shown. Similar results were obtained from PB or PNP, but are not shown here for clarity.



**Figure 8.** Current–voltage curve in 0.1:1 M KCl asymmetric solution from BD simulations (top) and PNP calculations (bottom). The total current (black) is the sum of  $K^+$  (magenta) and  $Cl^-$  (green) currents.

$I_{Cl}(-)$  than OmpF, resulting in almost no asymmetry in its channel conductance. Arg168 (and probably Arg167) located in the extracellular vestibule appears to be primarily responsible for the asymmetry in the channel conductance of wide-type OmpF. In contrast, K16A shows much higher outward  $K^+$  current  $I_K(+)$  and much lower outward  $Cl^-$  current  $I_{Cl}(+)$  than OmpF, resulting in larger asymmetry in the channel conductance. K16 located on the periplasmic side of the pore appears to play an important role in controlling outward currents. R132A has some intermediate effects, i.e. its effects for outward currents are close to K16A and those for inward currents are close to R168A.

In Figure 8 is shown the  $I$ – $V$  curves calculated from BD and PNP in the case of asymmetric salt solution of 0.1:1 M KCl. The reversal potential  $V_{rev}$  at zero net current is determined to be  $27.4(\pm 1.3)$  mV (BD) and  $22.1(\pm 0.6)$  mV (PNP), in excellent accord with the experimental value of 24.3 mV.<sup>6</sup> The results from PNP are qualitatively very reasonable, though the ion currents are slightly overestimated relative to BD. As discussed above, scaling down the diffusion constant of the ions inside the pore produces a similar  $I$ – $V$  relation to BD from PNP calculations. Such a scaling of the diffusion constants of both  $K^+$  and

$Cl^-$  changes only the slope of the  $I$ – $V$  curve but does not affect the value of the reversal potential. This suggests that the PNP approximation can be helpful to understand the dominant features of ion permeation and selectivity through OmpF. Interestingly, the  $I$ – $V$  curves calculated from both BD and PNP show that the current carried by each ionic species becomes nearly zero at its own Nernst equilibrium potential, as if the flux of one type of ion is not strongly affected by the flux of other ions. According to BD,  $I_K = 2.3(\pm 1.8)$  pA at  $+59.5$  mV and  $I_{Cl} = 0.5(\pm 1.1)$  pA at  $-59.5$  mV in 0.1:1 M KCl asymmetric solution, which are the Nernst potentials for a perfect cation or anion-selective pore. In PNP calculations, the  $K^+$  and  $Cl^-$  currents become identically zero at  $+59.5$  mV and  $-59.5$  mV, respectively. This follows from the fact that the NP equation (3) becomes the Nernst equation at  $I_\alpha = 0$ , regardless of the diffusion constant and type of channels (see also equation (12)). The value of the reversal potential is thus seen to follow directly from the sum of two currents of different magnitude that behave almost independently from one another, at least at a mean-field level. The value of the voltage at which the total current becomes zero is more or less determined by the relative magnitude of the two currents. It is customary to characterize the selectivity of ion channels in the framework of the Goldman–Hodgkin–Katz (GHK) voltage equation:<sup>19,50,51</sup>

$$V_{rev} = \frac{k_B T}{e} \ln \left[ \frac{P_K [C]_o + P_{Cl} [C]_i}{P_K [C]_i + P_{Cl} [C]_o} \right] \quad (6)$$

where  $[C]_i$  and  $[C]_o$  are the intracellular and extracellular KCl concentrations, i.e.  $[C]_i = 0.1$  M and  $[C]_o = 1$  M. On the basis of the above analysis, one might anticipate that the ratio of the currents at zero potential under asymmetric conditions of concentration  $|I_K/I_{Cl}|$  should be closely related to the ratio of the permeability coefficients  $P_K/P_{Cl}$ . The permeability ratios extracted from the GHK voltage equation are  $P_K/P_{Cl}$  are 3.9 (BD) and 2.9 (PNP). Remarkably, the calculated current ratios at zero potential are 3.4 (BD) and 2.4 (PNP), in excellent accord with the corresponding permeability ratios. In fact, it can be demonstrated that the permeability and current ratios are rigorously equivalent within the framework of GHK (see Appendix for details).

Such an apparent validity of the GHK voltage equation in the context of a complex molecular pore is surprising and intriguing. The GHK equations are derived using a one-dimensional Nernst–Planck (1D-NP) equation under the simplifying assumptions that the potential is linear over the length of the pore and that the diffusion coefficient is constant throughout the pore.<sup>19,50,51</sup> However, those assumptions are clearly not satisfied in the case of OmpF. First, as can be seen in Figure 9, there is a significant free energy barrier located in the constriction zone opposing the passage of  $K^+$  and  $Cl^-$  and the transmembrane

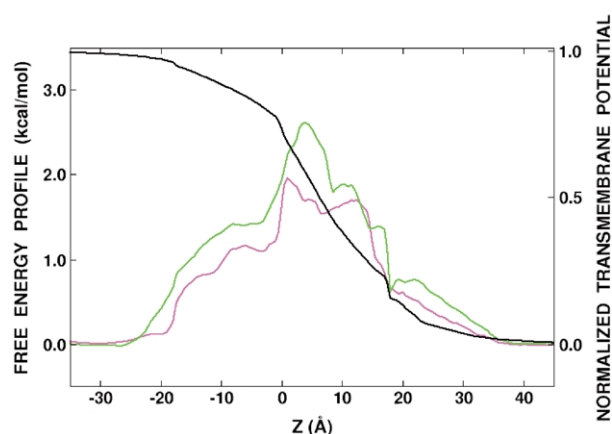


**Figure 9.** One-dimensional free energy profiles of  $K^+$  (magenta) and  $Cl^-$  (green) with the transmembrane potential of +150 mV (black). The value of 150 mV corresponds to 3.46 kcal/(mol e). The fraction of the transmembrane potential is also shown on the right. The free energy profiles of both ions were calculated as  $\mathcal{W}_\alpha(z) = -k_B T \ln(\rho_\alpha(z)/\rho_\alpha^{bulk})$  in a 1 M KCl symmetric solution, where  $\rho_\alpha(z)$  was calculated using a 0.5 Å bin along the Z-axis and the cross-sectional area of the BD system in the XY plane.

potential field across the pore is not linear. Second, the ion diffusion profiles are not constant inside the pore (see Figure 11). Furthermore, there are clear deviations from ion independence manifested as strong ion-counterion correlations as shown in Figure 6; the presence of a  $Cl^-$  in the narrowest part of the pore is almost always accompanied by a  $K^+$ . To help clarify those results, we formulated a simple model on the basis of the 1D-NP equation, but using slightly more realistic assumptions for the free energy profile and the transmembrane potential than those used to derive GHK. The details are given in Appendix. Using this simple model, it can be shown that the equivalence between the current and permeability ratios is preserved if the free energy barriers opposing the passage of cations and anions are located along the channel axis at a position where the transmembrane potential is roughly half of  $V_{mp}$ . As shown in Figure 9, this is the case for OmpF. Therefore, despite the presence of strong ion-ion correlations the system behaves as if there is some effective independence of the ion fluxes.

## Conclusion

We have performed an extensive study of the ion permeation properties of OmpF porin using MD and approximate approaches (BD, PB, and PNP). The different approaches were first compared by examining equilibrium properties in the particular case of a 1 M KCl symmetric salt solution. The present analysis shows that BD (explicit ions and continuum solvent) and PB (continuum ion densities and continuum solvent) both reproduce

quite well the main results from MD (explicit ions and water molecules). The average ion distributions inside the pore as well as the two distinct ion pathways along the pore calculated from all three approaches are remarkably consistent. This indicates that BD and PB are able to capture the important electrostatic interactions between ions and the charge distribution of the channel, and that the continuum dielectric solvent and the approximation of a rigid protein are valid in the case of OmpF.

BD and PNP were then compared in their ability to describe non-equilibrium ion flow through OmpF. The channel conductance in 0.2 M and 1 M KCl calculated from BD simulations is in excellent accord with the experimental data. It should be stressed that all the inputs for BD such as ion-exclusion hydration layer, ion diffusion profiles  $D_\alpha(z)$ , and the water-mediated short-range ion-ion interaction  $w_{sr}(r)$  were primarily extracted from MD<sup>9</sup> with no further adjustments to reproduce the experimental data. From this point of view, the quantitative agreement between the calculations with experimental data is particularly striking. The calculations also confirm the asymmetry in the channel conductance, i.e. higher conductance in positive transmembrane potential. The channel conductance of three mutants (R168A, R132A, and K16A) in 1 M KCl calculated from BD simulations suggests that the asymmetry in the OmpF channel conductance arises mostly from the permanent charge distribution of the channel. Arg168 (and also Arg167) appears to be primarily responsible for it.

Ion flow through OmpF is largely dependent on salt concentration. The present calculations reproduce the experimentally well-known conductance-concentration relation, i.e. the single-channel conductance normalized by salt concentration  $G/c$  increases with decreasing ionic strength.<sup>6</sup> Furthermore, the channel selectivity toward  $K^+$  ions (cations) increases with decreasing ionic strength due to reduction of ionic screening of the negative electrostatic potential arising from the protein charges.

Lastly, aspects of ion selectivity of OmpF were examined by calculating the non-equilibrium reversal potential using BD and PNP. The reversal potential is a challenging property to model quantitatively because of the difficulties in implementing realistic non-symmetric boundary conditions of ion concentration in BD simulations. In the present case, the boundary conditions were established by using the GCMC algorithm combined with BD.<sup>27</sup> From GCMC/BD and PNP, the reversal potential is calculated as 27.4(±1.3) mV (BD) and 22.1(±0.6) mV (PNP) for a tenfold salt gradient (0.1:1 M KCl), in excellent accord with the experimental value of 24.3 mV.<sup>6</sup> Interestingly, the present calculations show that the potential at which the current of one ionic species becomes zero is not strongly affected by the translocation of another type of ion as if there is some effective



independence of the ion fluxes. Nonetheless, examination of the BD trajectories reveals clear and obvious ion–ion correlations, in apparent contradiction with this observation.

In conclusion, the hierarchical approach in which all the inputs for the approximate approaches such as BD and PNP are obtained from the detailed MD appears to be robust in the case of OmpF porin. Overall, the results from BD quantitatively reproduce all the available experimental data very well. The results from PNP are qualitatively reasonable, though the channel conductance is typically overestimated by about 50% higher. Such inaccuracies are most likely due to the neglect of some dynamical ion–ion correlations in this mean-field theory. Application of this hierarchical approach in the case of the anion-selective phosphoporin (PhoE),<sup>12</sup> the cation-selective osmoporin (OmpK36),<sup>47</sup> and various OmpF mutants is currently in progress.

## Theory and Methods

All the OmpF models were constructed to have as close correspondence as possible. This is essential for a meaningful comparison of the different theoretical treatments. In particular, the ionization state of all titratable residues as well as all partial atomic charges attributed to the protein atoms was exactly the same in all the calculations. Furthermore, the BD, PB and PNP were on the basis of the same (fixed) channel structure as well as continuum dielectric representation of the water and membrane regions. Lastly, the ion-exclusion region (embodied by the core repulsive potential  $U_{\text{core}}(\mathbf{r})$ ) and the profile in the diffusion constant of the ions throughout the pore were the same in BD and PNP. In the following we provide a detailed description of the three theoretical models.

### OmpF porin atomic model

The atomic model has been described in detail.<sup>9</sup> Briefly, the initial configuration of the OmpF trimer was taken from the X-ray structure (PDB entry 2omf). The standard protonation state corresponding to pH 7 was used except for Glu296 and Asp312, which were protonated, so that the net charge of the OmpF trimer is  $-30e$ .<sup>6,9,45</sup> The trimer was centered at the origin and its threefold symmetry axis was directed along the Z-axis with the extracellular long loops at  $Z > 0$ . The center of a membrane bilayer is located at  $Z = 0$ . The position of OmpF ranges roughly from  $-24 \text{ \AA}$  to  $36 \text{ \AA}$  along the Z-axis.

### Molecular dynamics

An instantaneous configuration of the atomic model of the fully hydrated OmpF/DMPC system in 1 M KCl salt solution is shown in Figure 1.

It comprises the OmpF trimer, 124 DMPC lipid molecules (64 and 60 in the upper and lower leaflets of the bilayer, respectively), 134,70 water molecules (including 330 crystallographic water), 231  $\text{K}^+$  and 201  $\text{Cl}^-$ , for a total of 70,693 atoms. Hexagonal periodic boundary conditions were applied to represent an infinite planar bilayer in the XY direction with a center-to-center distance of  $99.88 \text{ \AA}$  between the neighboring trimers and to simulate a periodic multi-layer system along the Z-axis with a initial translation distance of  $83.0 \text{ \AA}$ . The center of the DMPC membrane bilayer is located at  $Z = 0$ .

The construction and equilibration of the complete OmpF system have been described in detail.<sup>9</sup> Briefly, after 350 ps equilibration, a 5 ns MD trajectory of the OmpF system was generated with 2 fs integration time step at constant normal pressure (1 atm), temperature (330 K), and cross-sectional surface area in the CPTA ensemble. Thus, the system's area is fixed but the height along the Z-axis changes to maintain the normal pressure.<sup>52,53</sup> The temperature was chosen to insure a fluid liquid-crystalline  $L_\alpha$  phase for the DMPC membrane.<sup>54</sup> All calculations were performed using the CHARMM biomolecular simulation program.<sup>55</sup> The all-atom parameter set PARAM22 for protein<sup>56</sup> and phospholipids,<sup>57</sup> and a modified TIP3P water model<sup>58</sup> were used. The Lennard–Jones (LJ) parameters for  $\text{K}^+$  and  $\text{Cl}^-$  were adjusted to yield the experimental solvation free energy in bulk water.<sup>59,60</sup> All bond lengths involving hydrogen atoms were fixed using the SHAKE algorithm.<sup>61</sup> Electrostatic interactions were calculated using the Particle–Mesh Ewald method to remove the artifact associated with truncation of electrostatic forces,<sup>62</sup> while the van der Waals energy was smoothly switched off at  $8\text{--}10 \text{ \AA}$  by use of a switching function.<sup>63</sup> The equilibration and the initial 2 ns production were calculated using 32 CPUs running in parallel on the IBM SP2 at the Cornell Theory Center (CTC). The following 3 ns production was calculated using 16 CPUs on the Origin 2000 at the National Center for Supercomputing Applications (NCSA). The atomic coordinates were saved every 50 step (100 fs) for analysis, producing 42.4 GB of data. A 50 ps production run took about 30 hours on the SP2 and 33 hours on the Origin 2000.

### Brownian dynamics

The multi-ion PMF  $\mathcal{W}$  in equation (2) takes into account the interactions between all the ions present in the simulation region, the influence of the channel, the transmembrane potential as well as implicit salt in the outer region. For the sake of simplicity, we choose to represent the solvent as a structureless dielectric medium and incorporate its influence implicitly.<sup>27,29</sup> It follows that the

multi-ion PMF is:

$$\begin{aligned} \mathcal{W}(\mathbf{R}_1, \mathbf{R}_2, \dots) \\ = \sum_{\alpha\gamma} \sum_{ij} u_{\alpha\gamma}(|\mathbf{r}_\alpha^{(i)} - \mathbf{r}_\gamma^{(j)}|) + \sum_{\alpha,i} U_{\text{core}}(\mathbf{r}_\alpha^{(i)}) \\ + \Delta\mathcal{W}_{\text{sf}}(\mathbf{R}_1, \mathbf{R}_2, \dots) + \Delta\mathcal{W}_{\text{rf}}(\mathbf{R}_1, \mathbf{R}_2, \dots) \end{aligned} \quad (7)$$

where the cartesian coordinates of the  $n_\alpha$  ions of type  $\alpha$  are represented by  $\mathbf{R}_\alpha \equiv (\mathbf{r}_\alpha^{(1)}, \mathbf{r}_\alpha^{(2)}, \dots, \mathbf{r}_\alpha^{(n_\alpha)})$ ,  $u_{\alpha\gamma}$  is the direct ion-ion interaction,  $U_{\text{core}}$  is a repulsive potential preventing core-core overlap of the ions with the channel and membrane,  $\Delta\mathcal{W}_{\text{sf}}$  is the shielded static external field coming from the permanent protein charge distribution and the transmembrane potential, and  $\Delta\mathcal{W}_{\text{rf}}$  is the reaction field arising from the electrostatic polarization of the various dielectric boundaries and the implicit salt in the outer region. The transmembrane potential contribution is calculated with a modified PB equation.<sup>64</sup> In all the calculations the transmembrane potential was set relative to the extracellular side. For the detailed description of each contribution to the PMF, the reader is referred to Im *et al.*<sup>27</sup> and Im & Roux.<sup>29</sup>

The direct interaction between two ions separated by a distance  $r$  is:

$$\begin{aligned} u_{\alpha\gamma}(r) = 4\epsilon_{\alpha\gamma} \left[ \left( \frac{\sigma_{\alpha\gamma}}{r} \right)^{12} - \left( \frac{\sigma_{\alpha\gamma}}{r} \right)^6 \right] + \frac{q_\alpha q_\gamma}{\epsilon_{\text{bulk}} r} \\ + w_{\text{sr}}(r) \end{aligned} \quad (8)$$

where  $\epsilon_{\alpha\gamma}$  and  $\sigma_{\alpha\gamma}$  are the parameters of the LJ 6-12 potential,  $q_\alpha$  and  $q_\gamma$  are the charge of the ions, and  $\epsilon_{\text{bulk}} = 80$  is the dielectric constant of bulk water. The first two terms in equation (8) correspond to the well-known restricted primitive model with soft core which has been frequently used in statistical mechanical studies of ionic solutions.<sup>65-68</sup> However, the primitive model cannot describe properly the structuring effects such as ion pairing arising from the granularity of the water molecules.<sup>69,70</sup> A water-mediated short-range ion-ion interaction  $w_{\text{sr}}(r)$  with a form of damped oscillations is incorporated into the primitive model to take into account the hydration effect:<sup>69,71</sup>

$$w_{\text{sr}}(r) = c_0 \exp \left[ \frac{c_1 - r}{c_2} \right] \cos[c_3(c_1 - r)\pi] + c_4 \left( \frac{c_1}{r} \right)^6 \quad (9)$$

A similar form has been used by Chung and co-workers for BD simulations.<sup>10,28</sup> A 2 ns MD simulation of a 1 M KCl aqueous salt solution was used to determine the coefficients  $c_0 - c_4$  for  $\text{K}^+ - \text{Cl}^-$ ,  $\text{K}^+ - \text{K}^+$ , and  $\text{Cl}^- - \text{Cl}^-$  pairs. Monte Carlo (MC) simulations were performed for a spherical 1 M KCl ionic solution of 25 Å with one  $\text{K}^+$  or one  $\text{Cl}^-$  kept fixed at the origin. The coefficients were empirically adjusted until a reasonable agreement was achieved between the radial distribution functions (RDF)  $g(r)$  of each pair calculated,

**Table 3.** Coefficients for the short-range ion-ion interaction function  $w_{\text{sr}}$

Pairs	$c_0$	$c_1$	$c_2$	$c_3$	$c_4$
$\text{K}^+ - \text{Cl}^-$	-3.70	2.90	0.90	0.75	0.00
$\text{K}^+ - \text{K}^+$	-0.60	4.40	0.90	0.80	0.25
$\text{Cl}^- - \text{Cl}^-$	-0.50	4.90	0.90	0.80	0.25

respectively, from the MC simulations and from the MD simulation. The final set of the coefficients for  $w_{\text{sr}}$  is given in Table 3. In Figure 10, all the RDFs calculated from BD are compared with those from MD.

Because the ion-accessible cross-sectional area along the channel pore plays an important role in the calculation of channel conductance,<sup>7</sup> its determination must be done carefully. Following the approach developed previously for the optimized PB atomic radii for proteins,<sup>72</sup> a set of ion-exclusion radii for protein in KCl salt solutions was determined from a 5 ns MD trajectory of OmpF in 1 M KCl salt solution;<sup>9</sup> 0.75 Å for all nitrogen atoms, 0.93 Å for all oxygen atoms, and 1.0 Å for all other heavy atoms. This was done by calculating radial ion distributions around specific atoms of some selected residues and by comparing with the distributions and the PB atomic radii

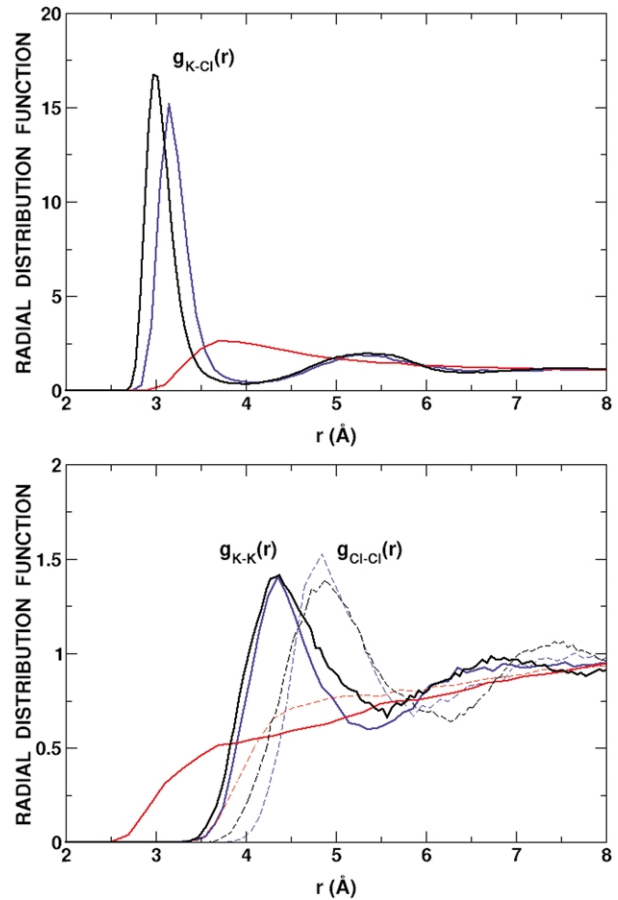


**Figure 10.** Ion-ion radial distribution functions from MD (black), BD with the short-range ion-ion interaction  $w_{\text{sr}}$  (blue), BD with the primitive model (red).

(data not shown). The PB radii augmented by the hydration radii layers were used to setup the molecular surface by which a core repulsion potential map  $U_{\text{core}}(\mathbf{r})$  was built and stored on a grid ( $101 \times 101 \times 181$  with a grid-spacing of  $0.5 \text{ \AA}$ ).  $U_{\text{core}}(\mathbf{r})$  is set to zero in all ion-accessible region and  $+50 \text{ kcal/mol}$  otherwise. The core repulsive energy and forces were calculated using a third-order B-spline interpolation.<sup>27</sup> Because the present interpolation scheme makes the ion-exclusion region extend roughly a half of the grid-spacing further from the protein ( $0.25 \text{ \AA}$ ), this distance is subtracted from the ion-exclusion radii.

An atomic system was constructed to perform GCMC/BD simulations<sup>27,29</sup> with an orthorhombic region ( $44.5 \text{ \AA} \times 44.5 \text{ \AA} \times 86.5 \text{ \AA}$ ) corresponding roughly to one OmpF monomer. The same protonation states as in the MD simulation were used and the atomic charges were taken from the all-atom PARAM22 force field<sup>56</sup> in CHARMM.<sup>55</sup> The static field electrostatic potential arising from the protein charges was calculated with the OmpF trimer model embedded in an ion-impermeable planar membrane of  $34 \text{ \AA}$  thickness centered at  $Z = 0$ . The influence of the transmembrane potential was also incorporated into the calculation of the electrostatic potential for non-equilibrium GCMC/BD simulations.<sup>27,29,64</sup> A dielectric constant of 2 was used for the interior of the protein and membrane regions. A dielectric constant of 80 was assumed for the bulk solvent region including the aqueous pore region of OmpF. The PB radii for proteins were used to setup the dielectric boundary.<sup>72</sup> A Debye–Hückel screening factor  $\kappa^2$  corresponding to given salt concentrations was assigned only into the outer region. The electrostatic potential was first calculated with a coarse grid ( $101^3$  points with a grid-spacing of  $1.5 \text{ \AA}$ ) centered on the entire OmpF trimer with periodic boundary conditions imposed in the X and Y directions. The result of the coarse calculation was then used to set the potential on the edge of a smaller box to perform a second calculation using a finer grid ( $101 \times 101 \times 181$  with a grid-spacing of  $0.5 \text{ \AA}$ ) centered on the orthorhombic simulation region corresponding roughly to one OmpF monomer. The electrostatic energy and forces were calculated using a second-order B-spline (trilinear) interpolation.<sup>27,73</sup> The same computational procedure (with all protein charges turned off and without transmembrane potential) was used to calculate the reaction field matrix  $\mathbf{M}^*$  for a total of 225 basis functions generated from all combination of the 5,

5, and 9 Legendre polynomials in X, Y, and Z directions, respectively. The basis set  $\{b_n(\mathbf{r})\}$  supports the ion charge density only in the ion-accessible space of the simulation region. Due to the inaccuracy near the (implicit salt) boundary in the basis-set expansion method,<sup>29</sup> for concentration higher than  $0.1 \text{ M}$ , we used only a reaction field matrix  $\mathbf{M}^*$  which was calculated with  $0.1 \text{ M}$  salt concentration assigned into the outer region. The reaction field electrostatic energy and forces are calculated at each time-step by updating the generalized multipole moments  $Q_n = \sum_{\alpha i} q_{\alpha} b_n(\mathbf{r}_{\alpha}^{(i)})$  (for details, see Im & Roux<sup>29</sup>). All continuum electrostatic calculations were performed using the PBEQ/GSBB module<sup>29,64,72–74</sup> of CHARMM.<sup>55</sup>

To maintain external electrochemical conditions two buffer regions were implemented in the periplasmic side (buffer 1;  $-37.75 \text{ \AA} < Z < -35.5 \text{ \AA}$ ) and in the extracellular side (buffer 2;  $+46.5 \text{ \AA} < Z < +48.75 \text{ \AA}$ ). The ions in the buffer regions are kept in equilibrium with the bulk solution with which they are in contact. This is enforced *via* the GCMC algorithm with particle creations and destructions only in the buffer regions.<sup>27</sup> The algorithm can be used to simulate equilibrium as well as non-equilibrium conditions of ion diffusion and permeation.<sup>27,29</sup> For the detailed description of the GCMC algorithm, the reader is referred to Im *et al.*<sup>27</sup> Because incorporating  $w_{\text{sr}}$  into the primitive model changes the nature of ion–ion interactions, the excess chemical potential  $\Delta\mu$  in  $1 \text{ M KCl}$ , previously calculated on the basis of the primitive model for GCMC calculations, was recalculated as:

$$\Delta\mu' = \Delta\mu - \frac{1}{k_B T} \ln \left[ \frac{\rho'(r)}{\rho(r)} \right] \quad (10)$$

where  $\Delta\mu'$  is the excess chemical potential with  $w_{\text{sr}}$ ,  $\Delta\mu$  is the excess chemical potential without  $w_{\text{sr}}$ ,  $\rho'(r)$  and  $\rho(r)$  are densities of  $\text{K}^+$  or  $\text{Cl}^-$  at large distance ( $r > 15 \text{ \AA}$ ), which are, respectively, obtained from BD simulations with and without  $w_{\text{sr}}$ , and with  $\Delta\mu$ . In this study, assuming that  $w_{\text{sr}}$  does not depend on ion concentration,  $\Delta\mu'$  in other concentrations were similarly calculated. All ion parameters are given in Table 4. To examine the current–voltage (*IV*) relation at different concentrations, in both buffer regions implemented were  $0.01 \text{ M}$ ,  $0.1 \text{ M}$ , and  $1 \text{ M KCl}$  (symmetric) solutions with the transmembrane potential  $V_{\text{mp}} = -150 \text{ mV}$ ,  $-100 \text{ mV}$ ,  $-50 \text{ mV}$ ,  $+50 \text{ mV}$ ,  $+100 \text{ mV}$ ,  $+150 \text{ mV}$ . To examine the conductance–concentration

**Table 4.** Ion parameters

Ion	$\epsilon^a$ (kcal/mol)	$\sigma^a$ ( $\text{\AA}$ )	$\Delta\mu'$ (kcal/mol)						
			2.0 M	1.0 M	0.5 M	0.3 M	0.2 M	0.1 M	0.01 M
$\text{K}^+$	0.0870	3.142645	−0.52097	−0.4325	−0.3568	−0.3010	−0.2573	−0.18243	−0.0617
$\text{Cl}^-$	0.1500	4.044680	−0.54552	−0.4570	−0.3684	−0.3076	−0.2615	−0.18435	−0.0618

<sup>a</sup> Taken from Roux.<sup>60</sup>



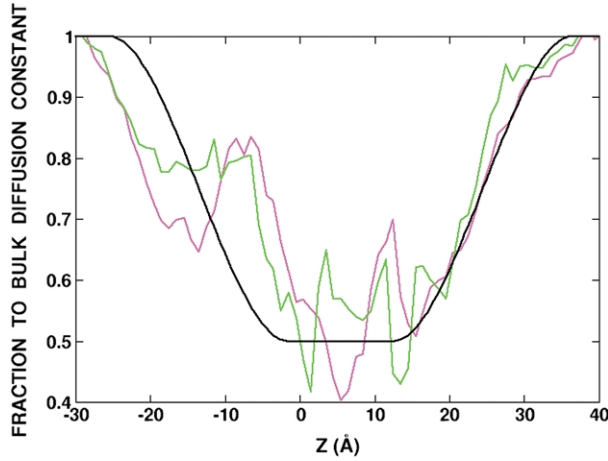


**Figure 11.** A (fractional) non-uniform diffusion constant profile for  $K^+$  and  $Cl^-$  in BD and PNP; 1 when  $z > 36.5$  or  $z < -25.5$ ,  $0.5(f_{\min})$  when  $-1.5 < z < 12.5$ , and  $f_{\min} + (1 - f_{\min})g_{sw}$  in switching regions, where a switching function centered at  $z_c = 5.5$  over  $L = 24$  Å length,  $g_{sw} = \pm 2((z - z_c)/L)^3 - 3((z - z_c)/L)^2$ , is applied. For comparison, the MD results for  $K^+$  (magenta) and  $Cl^-$  (green) scaled by their bulk values are also shown. We used  $0.196$  ( $K^+$ ) Å<sup>2</sup>/ps and  $0.203$  ( $Cl^-$ ) Å<sup>2</sup>/ps for the bulk diffusion constant.<sup>19</sup>

relation, the single-channel conductance was calculated at  $V_{mp} = \pm 150$  mV in 0.2 M, 0.3 M, 0.5 M, and 2 M KCl (symmetric) solutions. To calculate the reversal potential, a tenfold salt gradient was established between buffer 1 (0.1 M KCl) and buffer 2 (1 M KCl) regions (an asymmetric solution of 0.1:1 M KCl) with  $V_{mp} = -25$  mV, 0 mV, +25 mV, +50 mV, +75 mV.

The position-dependent diffusion constant of ions,  $D_\alpha(\mathbf{r})$ , in equation (2), is a central input parameter in many theoretical description of permeation.<sup>27,29,38,75–78</sup> In Figure 11, the diffusion constant profiles as a fraction to bulk values along the channel axis, which were obtained from MD simulation at 1 M KCl,<sup>9</sup> are compared with a (fractional) non-uniform analytical function which was used for  $K^+$  and  $Cl^-$  in both BD and PNP. For the sake of simplicity, the variations of ion diffusion constants in the XY plane as well as the small decrease in the diffusion constant of  $K^+$  and  $Cl^-$  as a function of salt concentration (about 2%)<sup>49</sup> are neglected in the present treatment. When  $D_\alpha(\mathbf{r})$  is non-uniform, its gradient must be incorporated into the BD algorithm (equation (2):<sup>31</sup>)

$$\dot{\mathbf{r}}_\alpha^{(i)}(t) = -\frac{D_\alpha(\mathbf{r})}{k_B T} \frac{\partial \mathcal{W}(\mathbf{r})}{\partial \mathbf{r}_\alpha^{(i)}} + \frac{\partial D_\alpha(\mathbf{r})}{\partial \mathbf{r}_\alpha^{(i)}} + \boldsymbol{\zeta}_\alpha^{(i)}(t) \quad (11)$$

where  $\boldsymbol{\zeta}_\alpha^{(i)}$  is a gaussian random noise with  $\langle \boldsymbol{\zeta}_\alpha^{(i)}(t) \cdot \boldsymbol{\zeta}_\alpha^{(j)}(0) \rangle = 6D_\alpha(\mathbf{r})\delta_{ij}(t)$ .

The GCMC/BD simulations were generated with a time-step of 15 fs; one step of GCMC was performed for each step of BD. The total length of each simulation was 1.5 μs (0.01 M), 1.2 μs (0.1 M), 0.9 μs (0.2 M), 0.9 μs (0.3 M), 0.6 μs (0.5 M), 0.45 μs (1 M), and 0.225 μs (2 M) for various

symmetric solutions and 0.9 μs for the asymmetric solution. Longer simulations in low ion concentrations are needed for better statistical convergence. To obtain statistical convergence on the ion currents at given voltages, ten independent GCMC/BC simulations were generated with both different initial configuration and different seed numbers for the random number generator. A GCMC/BD simulation took about 52 (0.2 M) to 78 (2 M) hours (CPU time) for the symmetric solution and about 87 hours (CPU time) for the asymmetric solution on a single Pentium III 1 GHz processor.

### Poisson–Nernst–Planck (PNP) electrodiffusion theory

To solve the coupled PNP equations (3) and (4), the flux density  $\mathbf{J}_\alpha(\mathbf{r})$  in equation (3) is re-written as:

$$\mathbf{J}_\alpha(\mathbf{r}) = -D_\alpha(\mathbf{r})e^{-\mathcal{W}_\alpha^{\text{eff}}(\mathbf{r})/k_B T} \nabla \left[ C_\alpha(\mathbf{r})e^{\mathcal{W}_\alpha^{\text{eff}}(\mathbf{r})/k_B T} \right] \quad (12)$$

Equation (12) is then transformed to the Laplace equation assuming that the system is at a steady-state, i.e.  $\nabla \cdot \mathbf{J}_\alpha = 0$ .<sup>38,79</sup>

$$\nabla \cdot [\bar{D}_\alpha(\mathbf{r}) \nabla \bar{C}_\alpha(\mathbf{r})] = 0 \quad (13)$$

where  $\bar{D}_\alpha(\mathbf{r}) = D_\alpha(\mathbf{r})e^{-\mathcal{W}_\alpha^{\text{eff}}(\mathbf{r})/k_B T}$  and  $\bar{C}_\alpha(\mathbf{r}) = C_\alpha(\mathbf{r})e^{\mathcal{W}_\alpha^{\text{eff}}(\mathbf{r})/k_B T}$ . The total effective potential  $\mathcal{W}_\alpha^{\text{eff}}(\mathbf{r})$  is the sum of non-electrostatic potential energy  $U_{\text{core}}(\mathbf{r})$  and electrostatic potential energy,  $q_\alpha \phi(\mathbf{r})$ . Kurnikova *et al.* pointed out that equation (13) is isomorphic to the Poisson equation (4).<sup>38</sup> For this reason, both equations can be solved numerically in a self-consistent manner on a discrete 3D-grid using similar finite-difference relaxation method.<sup>80–82</sup> In the present study, it is assumed that the non-electrostatic potential  $U_{\text{core}}(\mathbf{r})$  in equation (3) simply corresponds to the (hard-wall) repulsive potential by the channel and membrane which prevents the ions from going through the wall. (In practice, instead of handling  $U_{\text{core}}(\mathbf{r})$  explicitly, the repulsive potential is implemented by setting  $C_\alpha(\mathbf{r}) = 0$  to zero in non-ion-accessible regions and setting any components of  $\mathbf{J}_\alpha(\mathbf{r})$  to zero when any neighboring grid points which surrounds an ion-accessible region are not ion-accessible.<sup>38,79</sup>

Assuming that the channel axis is directed along the Z-axis and periodic boundary conditions are applied for potential and concentrations in the X and Y directions, the individual ion current is calculated from the ion flux  $\mathbf{J}_\alpha(\mathbf{r})$  as:

$$I_\alpha(z) = q_\alpha \int dx \int dy \hat{z} \cdot \mathbf{J}_\alpha(x, y, z) \quad (14)$$

where  $\hat{z}$  is a unit vector along the Z-axis. The total current is simply the sum of the current carried by each ion species  $\alpha$ . Because the ion current  $I_\alpha$  should be independent of  $z$  if a stationary flux is established, the accuracy of the numerical calculation can be assessed by the variation of  $I_\alpha$  as a

function of  $z$  (poorly converged results normally give rise to numerical variations of  $I(z)$ ).

The same protonation states as in the MD and BD simulations were used and the atomic charges were taken from the PARAM22 force field<sup>56</sup> in CHARMM.<sup>55</sup> An ion-accessible 3D-grid map was first constructed with a  $191^3$  grid with a grid-spacing of 0.5 Å centered on the OmpF trimer model embedded in an ion-impermeable planar membrane of 34 Å thickness centered at  $Z = 0$ . To have the same ion-accessible region in BD and PNP (or PB) as much as possible, the PB radii augmented by the ion-exclusion hydration layers were used to setup the molecular surface. This is important for a meaningful comparison of MD, BD, and PB in equilibrium. For example, when ion-ion and ion-channel interactions are turned off, both BD and PB give almost the same number of ions inside the pore; 3.3  $K^+$  (BD) and 3.6  $K^+$  (PB). The dielectric boundary was constructed with the same  $191^3$  grid using the PB radii. The same dielectric constants as in the BD simulations were used; 80 for water and 2 for protein and membrane. To setup the boundary potential on the top and bottom of the grid, the Debye-Hückel approximation was used for the Poisson equation (4). Assuming that the boundary points are in equilibrium with the bulk solution beyond the grid along the  $Z$ -axis, boundary concentrations in the steady-state NP equation (13) were calculated as:

$$C_\alpha(\mathbf{r}) = C_\alpha^{\text{bulk}} e^{-U_{\text{core}}(\mathbf{r})/k_B T} e^{-(q_\alpha \phi(\mathbf{r}) - \Theta q_\alpha V_{\text{mp}})/k_B T} \quad (15)$$

where  $\Theta$  is equal to zero for top grid-points ( $Z > 0$ ) and one for bottom grid-points ( $Z < 0$ ).

One cycle of a PNP iteration consists of solving the Poisson equation (4) for electrostatic potential and then the steady-state NP equation (13) for concentration of each ion type. Both equations are solved completely at each step of PNP iterations with tolerance values of  $2.0 \times 10^{-6}$  for potential and  $5.0 \times 10^{-11}$  for concentrations. To ensure the numerical stability during PNP iterations, performing a mixing of potential and concentrations in each step of iterations with ones in the previous iteration have implemented a relaxation method. For example, in  $n$ -th PNP iteration, the potential  $\phi^{(n)}(\mathbf{r})$  is mixed with the old potential  $\phi^{(n-1)}(\mathbf{r})$  with a mixing factor  $\lambda$  before solving the steady-state NP equation (13):

$$\phi^{(n)}(\mathbf{r}) = \lambda \phi^{(n)}(\mathbf{r}) + (1 - \lambda) \phi^{(n-1)}(\mathbf{r}) \quad (16)$$

Different mixing factors were applied to potential ( $\lambda = 0.02$ ) and concentrations ( $\lambda = 1.0$ ) because the steady-state NP equation (13) is very sensitive to small changes in potential, whereas the Poisson equation (4) is relatively insensitive to changes in concentrations. The linearized (or non-linear) PB equation was solved instead of the Poisson equation in the first PNP cycle and a reasonable initial guess of concentrations was then obtained for the steady-state NP equation (13) using

equation (15). Such a scheme helped significantly reduce both numerical instability and computational time. In the case of a highly charged protein such as OmpF porin, the potential obtained from PB is much closer to the correct answer than the unscreened potential from the Poisson equation without any background ion charge distribution.

The same diffusion constant profile  $D_\alpha(z)$  as in BD simulations was used (see Figure 11). The PNP calculations were performed on same boundary conditions (various symmetric solutions and an asymmetric solution), which were used for the BD simulations. Depending on the imposed conditions, a PNP calculation took about 15 (0.1 M) to 38 (0.5 M) hours (CPU time) on a single Pentium III 1 GHz processor. All calculations were done in a standalone program developed to solve the PNP equations for molecular pores of arbitrary geometry using the finite-difference method on the basis of the algorithm of Kurnikova *et al.*<sup>38</sup> (Im & Roux, unpublished).

## Acknowledgments

Useful discussions with Nathalie Saint and Toby Allen are gratefully acknowledged. We thank Ansgar Philippsen for his help with the DINO visualization program. This work was supported by the NIH grant R01-GM62342-01, Cornell Theory Center, and NCSA.

## References

1. Benz, R. & Bauer, K. (1988). Permeation of hydrophilic molecules through the outer membrane of Gram-negative bacteria. *Eur. J. Biochem.* **176**, 1–19.
2. Jap, B. & Wallan, P. (1990). Biophysics of the structure and functional of porins. *Quart. Rev. Biophys.* **23**, 367–403.
3. Nikaido, H. (1993). Transport across the bacterial outer membrane. *J. Bioenerg. Biomembr.* **25**, 581–589.
4. Benz, R., Schmid, A. & Hancock, R. (1985). Ion selectivity of Gram-negative bacterial porins. *J. Bacteriol.* **162**, 722–727.
5. Saint, N., Lou, K., Widmer, C., Luckey, M., Schirmer, T. & Rosenbusch, J. (1996). Structural and functional characterization of OmpF porin mutants selected for larger pore size. II. Functional characterization. *J. Biol. Chem.* **271**, 20676–20680.
6. Schirmer, T. & Phale, P. (1999). Brownian dynamics simulation of ion flow through porin channels. *J. Mol. Biol.* **294**, 1159–1167.
7. Phale, P., Philippsen, A., Widmer, C., Phale, V., Rosenbusch, J. & Schirmer, T. (2001). Role of charged residues at the OmpF porin channel constriction probed by mutagenesis and simulation. *Biochemistry*, **40**, 6319–6325.
8. Nikaido, H. (1992). Porin and specific channels of bacterial outer membranes. *Mol. Microbiol.* **6**, 435–442.
9. Im, W. & Roux, B. (2002). Ions and counterions in a biological channel: a molecular dynamics simulation

- of OmpF porin from *Escherichia coli* in an explicit membrane with 1 M KCl aqueous salt solution. *J. Mol. Biol.* **319**, 1177–1197.
10. Moy, G., Corry, B., Kuyucak, S. & Chung, S. (2000). Test of continuum theories as models of ion channels. I. Poisson–Boltzmann theory *versus* Brownian dynamics. *Biophys. J.* **78**, 2349–2363.
  11. Corry, B., Kuyucak, S. & Chung, S. (2000). Test of continuum theories as models of ion channels. II. Poisson–Nernst–Planck theory *versus* Brownian dynamics. *Biophys. J.* **78**, 2364–2381.
  12. Cowan, S., Schirmer, T., Rummel, G., Steiert, M., Ghosh, R., Pauptit, R. *et al.* (1992). Crystal structures explain functional properties of two *E. coli* porins. *Nature*, **358**, 727–733.
  13. Schirmer, T. (1998). General and specific porins from bacterial outer membranes. *J. Struct. Biol.* **121**, 101–109.
  14. Koebnik, R., Locher, K. & van Gelder, P. (2000). Structure and function of bacterial outer membranes: barrels in a nutshell. *Mol. Microbiol.* **37**, 239–253.
  15. Miyazawa, A., Fujiyoshi, Y., Stowell, M. & Unwin, N. (1999). Nicotinic acetylcholine receptor at 4.6 Å resolution: transverse tunnels in the channel wall. *J. Mol. Biol.* **288**, 765–786.
  16. Sokolova, O., Kolmakova-Partensky, L. & Grigorieff, N. (2001). Three-dimensional structure of a voltage-gated potassium channel at 2.5 nm resolution. *Structure*, **9**, 215–220.
  17. Jiang, Y., Lee, A., Chen, J., Cadene, M., Chait, B. & MacKinnon, R. (2002). The open pore conformation of potassium channels. *Nature*, **417**, 523–526.
  18. Chung, S., Allen, T. & Kuyucak, S. (2002). Modeling diverse range of potassium channels with Brownian dynamics. *Biophys. J.* **83**, 263–277.
  19. Hille, B. (2001). *Ion Channels of Excitable Membranes*, 3rd edit., Sinauer, Sunderland, MA.
  20. Allen, M. & Tildesley, D. (1989). *Computer Simulation of Liquids*, Oxford Science Publications, Clarendon Press, Oxford.
  21. Suenaga, A., Komeiji, Y., Uebayasi, M., Meguro, T., Saito, M. & Yamato, I. (1998). Computational observation of an ion permeation through a channel protein. *Biosci. Rep.* **18**, 39–47.
  22. Tieleman, D. & Berendsen, H. (1998). A molecular dynamics study of the pores formed by *Escherichia coli* OmpF porin in a fully hydrated palmitoyl-oleoylphosphatidylcholine bilayer. *Biophys. J.* **74**, 2786–2801.
  23. Tieleman, D., Biggin, P., Smith, G. & Sansom, M. (2001). Simulation approaches to ion channel structure–function relationships. *Quart. Rev. Biophys.* **34**, 473–561.
  24. Roux, B. (2002). Theoretical and computational models of ion channels. *Curr. Opin. Struct. Biol.* **12**, 182–189.
  25. Chung, S., Hoyles, M., Allen, T. & Kuyucak, S. (1998). Study of ionic currents across a model membrane channel using Brownian dynamics. *Biophys. J.* **75**, 793–809.
  26. Chung, S., Allen, T., Hoyles, M. & Kuyucak, S. (1999). Permeation of ions across the potassium channel: Brownian dynamics studies. *Biophys. J.* **77**, 2517–2533.
  27. Im, W., Seefeld, S. & Roux, B. (2000). A grand canonical Monte Carlo–Brownian dynamics algorithm for simulating ion channels. *Biophys. J.* **79**, 788–801.
  28. Corry, B., Allen, T., Kuyucak, S. & Chung, S. (2001). Mechanisms of permeation and selectivity in calcium channels. *Biophys. J.* **80**, 195–214.
  29. Im, W. & Roux, B. (2001). Brownian dynamics simulations of ions channels: a general treatment of electrostatic reaction fields for molecular pores of arbitrary geometry. *J. Chem. Phys.* **115**, 4850–4861.
  30. Chandrasekar, S. (1943). Stochastic problem in physics and astronomy. *Rev. Mod. Phys.* **15**, 1–89.
  31. Ermak, D. & McCammon, J. (1978). Brownian dynamics with hydrodynamics interactions. *J. Chem. Phys.* **69**, 1352–1360.
  32. Kirkwood, J. (1934). Theory of solutions of molecules containing widely separated charges with special application to zwitterions. *J. Chem. Phys.* **2**, 351–361.
  33. Roux, B. (1999). Statistical mechanical equilibrium theory of selective ion channels. *Biophys. J.* **77**, 139–153.
  34. Onsager, L. (1926). Zur theorie der elektrolyte (1). *Phys. Z.* **27**, 388–392.
  35. Onsager, L. (1927). Zur theorie der elektrolyte (2). *Phys. Z.* **28**, 277–298.
  36. Sharp, K. & Honig, B. (1990). Electrostatic interactions in macromolecules: theory and applications. *Annu. Rev. Biophys. Biophys. Chem.* **19**, 301–332.
  37. Roux, B. & Simonson, T. (1999). Implicit solvent models. *Biophys. Chem.* **78**, 1–20.
  38. Kurnikova, M., Coalson, R., Graf, P. & Nitzan, A. (1999). A lattice relaxation algorithm for three-dimensional Poisson–Nernst–Planck theory with application to ion transport through the gramicidin A channel. *Biophys. J.* **76**, 642–656.
  39. Tang, J., Chen, D., Saint, N., Rosenbusch, J. & Eisenberg, R. (1997). Permeation through porin and its mutant G119D. *Biophys. J.* **72**, A108.
  40. Levitt, D. (1999). Modeling of ion channels. *J. Gen. Physiol.* **113**, 789–794.
  41. McClesky, E. (1999). Calcium channel permeation: a field in flux. *J. Gen. Physiol.* **113**, 765–772.
  42. Miller, C. (1999). Ionic hopping defended. *J. Gen. Physiol.* **113**, 783–787.
  43. Nonner, W., Chen, D. & Eisenberg, B. (1999). Progress and prospects in permeation. *J. Gen. Physiol.* **113**, 773–782.
  44. Roux, B. (1999). Theories of ion permeation: a chaser. *J. Gen. Physiol.* **114**, 605–608.
  45. Karshikoff, A., Spassov, V., Cowan, S., Ladenstein, R. & Schirmer, T. (1994). Electrostatic properties of two porin channels from *Escherichia coli*. *J. Mol. Biol.* **240**, 372–384.
  46. Ranatunga, K., Adcock, C., Kerr, I., Smith, G. & Sansom, M. (1999). Ion channels of biological membranes: prediction of single channel conductance. *Theor. Chem. Accts*, **101**, 97–102.
  47. Dutzler, R., Rummel, G., Alberti, S., Hernandez-Alles, S., Phale, P., Rosenbusch, J. *et al.* (1999). Crystal structure and functional characterization of OmpK36, the osmoporin of *Klebsiella pneumoniae*. *Structure*, **7**, 425–434.
  48. Bredin, J., Saint, N., Malléa, M., Dé, E., Molle, G., Pagès, J.-M. & Simonet, V. (2002). Alteration of pore properties of *Escherichia coli* OmpF induced by mutation of key residues in anti-loop. *Biochem. J.* **363**, 521–528.
  49. Mills, R. & Lobo, V. (1989). *Self-diffusion in Electrolyte Solutions*, Elsevier, Amsterdam.
  50. Goldman, D. (1943). Potential, impedance and rectification in membranes. *J. Gen. Physiol.* **27**, 37–60.



51. Hodgkin, A. & Katz, B. (1949). The effect of sodium ions on the electrical activity of the giant axon of the squid. *J. Physiol.* **108**, 37–77.
52. Zhang, Y., Feller, S., Brooks, B. & Pastor, R. (1995). Computer simulation of liquid/liquid interfaces. I. Theory and application to octane/water. *J. Chem. Phys.* **103**, 10252–10266.
53. Feller, S., Zhang, Y., Pastor, R. & Brooks, B. (1995). Constant pressure molecular dynamics simulation—the Langevin piston method. *J. Chem. Phys.* **103**, 4613–4621.
54. Gennis, R. (1989). *Biomembranes: Molecular Structure and Functions*, Springer, New York.
55. Brooks, B., Brucoleri, R., Olafson, B., States, D., Swaminathan, S. & Karplus, M. (1983). CHARMM: a program for macromolecular energy minimization and dynamics calculations. *J. Comput. Chem.* **4**, 187–217.
56. MacKerell, A. J., Bashford, D., Bellot, M., Dunbrack, R., Evanseck, J., Field, M. *et al.* (1998). All-atom empirical potential for molecular modeling and dynamics studies of proteins. *J. Phys. Chem. B*, **102**, 3586–3616.
57. Schlenkrich, M., Brickmann, J., MacKerell, A. J. & Karplus, M. (1996). An empirical potential energy function for phospholipids: criteria for parameters optimization and applications. In *Biological Membranes. A Molecular Perspective from Computation and Experiment* (Merz, K. & Roux, B., eds), pp. 31–81, Birkhauser, Boston, MA.
58. Jorgensen, W., Chandrasekhar, J., Madura, J., Impey, R. & Klein, M. (1983). Comparison of simple potential functions for simulating liquid water. *J. Chem. Phys.* **79**, 926–935.
59. Beglov, D. & Roux, B. (1994). Finite representation of an infinite bulk system: solvent boundary potential for computer simulations. *J. Chem. Phys.* **100**, 9050–9063.
60. Roux, B. (1996). Valence selectivity of the gramicidin channel: a molecular dynamics free energy perturbation study. *Biophys. J.* **71**, 3177–3185.
61. Ryckaert, J., Ciccotti, G. & Berendsen, H. (1977). Numerical integration of the Cartesian equation of motions of a system with constraints: molecular dynamics of *n*-alkanes. *J. Comput. Chem.* **23**, 327–341.
62. Essmann, U., Perera, L., Berkowitz, M., Darden, T., Lee, H. & Pedersen, L. (1995). A smooth particle mesh Ewald method. *J. Chem. Phys.* **103**, 8577–8593.
63. Steinbach, P. & Brooks, B. (1994). New spherical-cut-off methods for long-range forces in macromolecular simulation. *J. Comput. Chem.* **15**, 667–683.
64. Roux, B. (1997). The influence of the membrane potential on the free energy of an intrinsic protein. *Biophys. J.* **73**, 2980–2989.
65. Ramanathan, P. & Friedman, H. (1971). Study of a refined model for aqueous 1-1 electrolytes. *J. Chem. Phys.* **54**, 1086–1099.
66. Ermak, D. (1975). A computer simulation of charged particles in solution. I. Technique and equilibrium properties. *J. Chem. Phys.* **62**, 4189–4196.
67. Wood, M. & Friedman, H. (1987). Brownian dynamics simulation of models for aqueous 1 M NaCl and 1/2 M CuSO<sub>4</sub>. *Z. Phys. Chem. Neue Folge Bd.* **155**, 121–132.
68. Jardat, M., Bernard, O., Turq, P. & Kneller, G. (1999). Transport coefficients of electrolyte solutions from smart Brownian dynamics simulations. *J. Chem. Phys.* **110**, 7993–7999.
69. Pettitt, B. & Rossky, P. (1986). Alkali halides in water: ion–solvent and ion–ion potential of mean force at infinite dilution. *J. Chem. Phys.* **84**, 5836–5844.
70. Llano-Restrepo, M. & Chapman, W. (1994). Monte Carlo simulation of the structural properties of concentrated aqueous alkali halide solutions at 25° using a simple civilized model. *J. Chem. Phys.* **100**, 8321–8339.
71. Guàrdia, E. & Pardr , J. (1991). Potential of mean force by constrained molecular dynamics: a sodium chloride ion-pair in water. *Chem. Phys.* **155**, 187–195.
72. Nina, M., Beglov, D. & Roux, B. (1997). Atomic radii for continuum electrostatics calculations based on molecular dynamics free energy simulations. *J. Phys. Chem. B*, **101**, 5239–5248.
73. Im, W., Beglov, D. & Roux, B. (1998). Continuum solvation model: electrostatic forces from numerical solutions to the Poisson–Boltzmann equation. *Comput. Phys. Commun.* **111**, 59–75.
74. Im, W., Bern che, S. & Roux, B. (2001). Generalized solvent boundary potential for computer simulations. *J. Chem. Phys.* **114**, 2924–2937.
75. Chiu, S., Novotny, J. & Jakobsson, E. (1993). The nature of ion and water barrier crossing in a simulated ion channel. *Biophys. J.* **64**, 98–109.
76. McGill, P. & Schumaker, M. (1996). Boundary conditions for single-ion diffusion. *Biophys. J.* **71**, 1723–1742.
77. Smith, G. & Sansom, M. (1999). Effective diffusion coefficients of K<sup>+</sup> and Cl<sup>−</sup> ions in ion channel models. *Biophys. Chem.* **79**, 129–151.
78. Allen, T., Kuyucak, S. & Chung, S. (2000). Molecular dynamics estimates of ion diffusion in model hydrophobic and KCSA potassium channels. *Biophys. Chem.* **86**, 1–14.
79. Cardenas, A., Coalson, R. & Kurnikova, M. (2000). Three-dimensional Poisson–Nernst–Planck theory studies: influence of membrane electrostatics on gramicidin A channel conductance. *Biophys. J.* **79**, 80–93.
80. Warwicker, J. & Watson, H. (1982). Calculation of the electric potential in the active site cleft due to alpha-helix dipoles. *J. Mol. Biol.* **157**, 671–679.
81. Klapper, I., Hagstrom, R., Fine, R., Sharp, K. & Honig, B. (1986). Focusing of electric fields in the active site of Cu–Zn superoxide dismutase: effects of ionic strength and amino-acid modification. *Proteins: Struct. Funct. Genet.* **1**, 47–59.
82. Nicholls, A. & Honig, B. (1991). A rapid finite difference algorithm, utilizing successive over-relaxation to solve the Poisson–Boltzmann equation. *J. Comput. Chem.* **12**, 435–445.

## Appendix

The diffusion of ions along the axis of a channel of length  $L$  is considered. The diffusion of the ions is described using the 1D-NP equation:<sup>19</sup>

$$J_{\alpha}(z) = -D_{\alpha}(z) \left( \frac{d}{dz} C_{\alpha}(z) + \frac{C_{\alpha}(z)}{k_B T} \frac{d}{dz} \mathcal{W}_{\alpha}(z) \right) \quad (A1)$$

where  $J_{\alpha}(z)$  is the flux density of the ion of type  $\alpha$ , and  $\mathcal{W}_{\alpha}(z)$  is the total free energy profile. In the context of GHK (linear field, i.e.  $\mathcal{W}_{\alpha}(z) = -q_{\alpha} V_{mp}(z/L - 1)$ , and constant diffusion

coefficient), the current is:

$$I_\alpha = P_\alpha \left( \frac{q_\alpha^2 V_{mp}}{k_B T} \right) \frac{[C_\alpha]_i - [C_\alpha]_o e^{-q_\alpha V_{mp}/k_B T}}{1 - e^{-q_\alpha V_{mp}/k_B T}} \quad (A2)$$

where  $P_\alpha = D_\alpha/L$  and  $C_\alpha(0) \equiv [C_\alpha]_i$  and  $C_\alpha(L) \equiv [C_\alpha]_o$ . Using these equations, it can be easily shown that  $P_K/P_{Cl} = |I_K/I_{Cl}|$  at zero potential in an asymmetric solution ( $[C_\alpha]_i \neq [C_\alpha]_o$ ) or at any applied potential in a symmetric solution ( $[C_\alpha]_i = [C_\alpha]_o$ ). We now extend this theory by assuming that the total free energy potential is given by:

$$\mathcal{W}_\alpha(z) = q_\alpha \phi_{mp}(z) + \mathcal{W}_\alpha^{(0)}(z) \quad (A3)$$

where  $\phi_{mp}(z)$  is the transmembrane potential profile along the pore, and  $\mathcal{W}_\alpha^{(0)}(z)$  is the voltage-independent contribution to the free energy profile of the ion. It is assumed that  $\phi_{mp}(0) = V_{mp}$ ,  $\phi_{mp}(L) = 0$ , and  $\mathcal{W}_\alpha^{(0)}(0) = \mathcal{W}_\alpha^{(0)}(L) = 0$ . Using this potential and those boundary conditions in the 1D-NP equation yields the average current  $I_\alpha = q_\alpha J_\alpha$ :

$$I_\alpha = q_\alpha P_\alpha^{(0)} \left\langle e^{q_\alpha \phi_{mp}(z)/k_B T} \right\rangle^{-1} \left( [C_\alpha]_i e^{q_\alpha V_{mp}/k_B T} - [C_\alpha]_o \right) \quad (A4)$$

where the permeability coefficient is:

$$P_\alpha^{(0)} = \left[ \int_0^L dz e^{+\mathcal{W}_\alpha^{(0)}(z)/k_B T} / D_\alpha(z) \right]^{-1} \quad (A5)$$

The voltage dependence appears in the form of a weighted average of an exponential factor over

the length of the pore:

$$\left\langle e^{q_\alpha \phi_{mp}(z)/k_B T} \right\rangle = \frac{\int_0^L dz e^{q_\alpha \phi_{mp}(z)/k_B T} e^{\mathcal{W}_\alpha^{(0)}(z)/k_B T} / D_\alpha(z)}{\int dz e^{\mathcal{W}_\alpha^{(0)}(z)/k_B T} / D_\alpha(z)} \quad (A6)$$

If the free energy profile is dominated by a single free energy barrier, the weighted average can be approximately written as:

$$\left\langle e^{q_\alpha \phi_{mp}(z)/k_B T} \right\rangle \approx e^{q_\alpha f_\alpha V_{mp}/k_B T} \quad (A7)$$

where  $f_\alpha$  is the fraction of the transmembrane potential. Assuming zero total current (stationary conditions), the reversal potential can then be expressed as:

$$V_{rev} = \frac{k_B T}{e} \ln \left[ \frac{P_K(V)[C]_o + P_{Cl}(V)[C]_i}{P_K(V)[C]_i + P_{Cl}(V)[C]_o} \right] \quad (A8)$$

where the effective voltage-dependent permeability coefficients are  $P_K(V) = P_K^{(0)} e^{-ef_K V_{mp}/k_B T}$  and  $P_{Cl}(V) = P_{Cl}^{(0)} e^{-e(1-f_{Cl})V_{mp}/k_B T}$ . From equation (A4), it can be shown that the current ratios  $|I_K/I_{Cl}|$  calculated at zero potential is nearly equivalent to the corresponding permeability ratio  $P_K/P_{Cl}$  if the value of the fraction of the transmembrane potential  $f_K$  and  $f_{Cl}$  are similar. Interestingly, the voltage-dependence of the effective permeability coefficient cancels out if  $f_K = f_{Cl} = 0.5$ , i.e. when the barrier is located approximately in the center of the membrane. According to Figure 9, this is verified in the case of OmpF.

*Edited by B. Honig*

(Received 20 February 2002; received in revised form 12 July 2002; accepted 24 July 2002)